Establishment of a Zr(IV) blood plasma model

T.V Basinyi

24009105

BSc (Hons), 2012 NWU

Dissertation submitted in partial fulfillment of the requirements for the degree Master of Science in Applied Radiation Science and Technology at the Mafikeng Campus of the North-West University

Supervisor: Prof. J.R. Zeevaart

Co-supervisor: Prof. V. Tshivhase

Submitted on April 2016

Declaration

I hereby declare that the Establishment of a Zirconium Blood Plasma Model presented in this dissertation is my own work and that all the sources I have used are indicated in the references. This mini-dissertation has never been submitted for a degree at any university before.

T.V. Basinyi

Signature: ……

Date : 22/04/2016

Acknowledgements

I would like to express my sincere gratitude to the following:

- My supervisors Prof Dr J.R Zeevaart, Miss L.C. Sepini, Prof V. Tshivhase and Dr D.R Jansen for their mentorship and guidance.

- North West University (CARST), for financial assistance.

- Necsa (Department of Radiochemistry), for offering me a suitable environment for doing my research.

- My family for believing in me and for their support over the years.

Abstract

This study was carried out in an effort to verify ^{89}Zr as a new safe and effective nuclide for immuno-PET imaging. In recent years, immuno-PET imaging has been of increasing importance in cancer diagnostics due to its rare abilities. This diagnostic tool has the ability to selectively target tumours thus allowing patients with cancers associated with poor prognosis to be identified in early stages of the disease. One of the cancers associated with poor prognosis is the epithelial ovarian cancer. At present, epithelial ovarian cancer is the fifth leading form of cancer resulting in deaths of women in the United States of America and possibly the rest of the world. The high mortality rate associated with epithelial ovarian cancer is the basis of this research because it shows that there is a need to develop effective tracers.

The stability and the in vivo robustness of the ^{89}Zr-DFO chelator system as part of potential immuno-PET radiopharmaceuticals was investigated by means of potentiometry and computer simulation of blood plasma. Glass electrode potentiometry was used to measure formation constants of the complexation of Zr^{4+} with DFO and the competing blood plasma ligands. This made the construction of the blood plasma model possible because the formation constants that were attained were used in ECCLES blood plasma model to evaluate the competitive stability of the ^{89}Zr-DFO chelator system against biological metal ions and ligands.

The results of the ECCLES blood plasma model showed that 99.7 % of Zr^{4+} ions will not dissociate from the ^{89}Zr-DFO complex when administered at a concentration of 8.5×10^{-5} $mol.dm^{-3}$.This was a positive result showing that almost all of the metal ions will reach the targeted area, however, the ligand on the other hand proved to be less stable resulting in a 10 % stability. The model showed that 88.6 % of the ligand will dissociate to form a complex with Fe^{3+} thus leading to a significant mobilization of the metal ion in the blood plasma.

Table of Contents

Declaration ii

Acknowledgements iii

Abstract iv

List of Figures viii

List of Tables xi

List of Abbreviations and Symbols xii

CHAPTER 1: INTRODUCTION 1

1.1 ZIRCONIUM 1

1.2 IMMUNO-PET 2

1.2.1 Principles of Immuno-PET 2

1.2.2 Appropriate Radionuclides for Immuno-PET 3

1.3 CHELATORS 6

1.4 STRUCTURE OF A RADIOMETAL-BASED PET TRACER 6

1.5 BENEFITS OF IMMUNO-PET 6

1.6 ^{89}Zr-LABELED ANTIBODIES IN CANCER THERAPY 8

1.7 EPITHELIAL OVARIAN CANCER (EOC) 8

1.8 OTHER MEDICAL APPLICATIONS 9

1.9 QUALITY CONTROL 10

1.10 RESEARCH OBJECTIVE 10

1.11 THESIS OUTLINE 12

REFERENCES 13

CHAPTER 2: THEORETICAL BACKGROUND 16

2.1 INTRODUCTION 16

2.2 POTENTIOMETRY 17

2.3 GLASS ELECTRODE POTENTIOMETRY (GEP) 19

2.4 MODELLING 20

2.4.1 ESTA1: the simulation mode 22

2.4.2 ESTA2: the optimization modules 24

2.4.3 ECCLES 24

REFERENCES 25

CHAPTER 3: EXPERIMENTAL 27
3.1 REAGENTS 27
3.2 METHODS 27
3.2.1 Preparations of Solutions 27
3.2.2 Experimental Set-up 28
3.3 GLASS ELECTRODE POTENTIOMETRY 29
3.3.1 Glass electrode calibration 29
3.3.2 Experimental Procedure 29
CHAPTER 4: RESULTS AND DISCUSSIONS 32
4.1 Zr^{4+} SOLUTION CHEMISTRY 32
4.1.1 Complexation 33
4.1.2 JESS computer program 34
4.2 AMINO ACIDS 35
4.3 GLUTAMINATE 36
4.3.1 Introduction 36
4.3.2 Results and discussions 36
4.3.3 Glutamine protonation (ionization) 38
4.3.4 Complexation of Zr(IV) with glutaminate 39
4.4 ASPARTATE 42
4.4.1 Introduction 42
4.4.2 Results and discussions 43
4.4.3 Aspartic acid protonation (ionization) 45
4.4.4 Complexation of Zr(IV) with aspartate 46
4.5 ASPARAGINATE 49
4.5.1 Introduction 49
4.5.2 Results and discussions 49
4.5.3 Asparagine protonation (ionization) 51
4.5.4 Complexation of Zr(IV) with asparagine 52

4.6 SALICYLIC ACID 56
4.6.1 Introduction 56
4.6.2 Results and discussions 56
4.6.3 Salicylic acid protonation (ionization) 57
4.6.4 Complexation of Zr(IV) with salicylic acid 59
4.7 CITRATE 61
4.7.1 Introduction 61
4.7.2 Results and discussions 62
4.7.3 Citric acid protonation (ionization) 63
4.7.4 Complexation of Zr(IV) with citric acid 65
4.8 DEFEROXAMINE 68
4.8.1 Introduction 68
4.8.2 Results and discussions 69
4.8.3 DFO-B protonation (ionization) 70
4.8.4 Complexation of Zr(IV) with DFO-B 71
4.9 BLOOD PLASMA SIMULATIONS 74
4.9.1 Introduction 74
4.9.2 Speciation in blood plasma 74
4.9.3 Blood plasma mobilization indexes 76
REFERENCES 78
CHAPTER 5: CONCLUSSION 80

List of Figures

Figure 1.1 An illustration of positron emission and annihilation [8]..... 2

Figure 1.2 An illustration of ^{89}Zr(IV) bound to a chelate (DFO) and attached to an antibody (Panitumumab) injected into a patient for a brain scan [10]..... 3

Figure 1.3 The structure of a radiometal-based PET tracer [17]..... 6

Figure 1.4 An illustration of the distinguishing capability of Immuno-PET regarding the HER2− and HER2+ tumours [19]..... 7

Figure 1.5 Images obtained from Immuno-PET/CT imaging study conducted at Jules Bordet Institute, comparing ^{89}Zr-rituximab with [18F] FDG-PET/CT in a patient with CD20+ Bcell lymphoma [26]..... 9

Figure 1.6 Structures of the ligands studied with Zr(IV)..... 11

Figure 2.1 Schematic diagram of a combination glass electrode for measuring pH [7].. 20

Figure 3.1 Photo of the experimental set-up used in this study..... 28

Figure 3.2 The experimental set-up in the titration vessel..... 29

Figure 4.1 Structure of the oligomer $Zr_4(OH)_8(H_2O)_{16}X_z^{(8-z)+}(aq)$ as deduced by Muha and Vaughn and reproduced from Baes and Mesmer..... 33

Figure 4.3.1 Structure of glutamine..... 36

Figure 4.3.2 $\overline{Z}_H$ curves for the protonation of glutamine..... 38

Figure 4.3.3 Speciation distribution curve for the protonation of glutamine plotted as a function of pH at 25 ^{o}C and 0.15 M NaCl..... 39

Figure 4.3.4 $\overline{Z}$ curves for the complexation of glutamine with Zr(IV)..... 40

Figure 4.3.5 $\overline{Q}$ curves for the complexation of glutamine with Zr(IV)..... 41

Figure 4.3.6 Speciation distribution curve of Zr(IV) complexation by glutaminate plotted as a function of pH at 25 ^{o}C and 0.15 M NaCl..... 42

Figure 4.4.1 Structure of aspartic acid..... 43

Figure 4.4.2 $\overline{Z}_{H}$ curves for the protonation of aspartic acid 45

Figure 4.4.3 Speciation distribution curve for the protonation of aspartic acid plotted as a function of pH at 25 °C and 0.15 M NaCl..... 46

Figure 4.4.4 $\overline{Z}$ curves for the complexation of aspartate with Zr(IV)..... 46

Figure 4.4.5 $\overline{Q}$ curves for the complexation of aspartate with Zr(IV)..... 47

Figure 4.4.6 Speciation distribution curve of Zr(IV) complexation by aspartic acid plotted as a function of pH at 25 °C and 0.15 M NaCl..... 48

Figure 4.5.1 Structure of asparagine..... 49

Figure 4.5.2 $\overline{Z}_{H}$ curves for the protonation of asparagine..... 51

Figure 4.5.3 Speciation distribution curve for the protonation of asparagine plotted as a function of pH at 25 °C and 0.15 M NaCl..... 52

Figure 4.5.4 $\overline{Z}$ curves for the complexation of asparagine with Zr(IV)..... 53

Figure 4.5.5 $\overline{Q}$ curves for the complexation of asparagine with Zr(IV)..... 54

Figure 4.5.6 Speciation distribution curve of Zr(IV) complexation by asparaginate plotted as a function of pH at 25 °C and 0.15 M NaCl..... 55

Figure 4.6.1 Structure of salicylic acid..... 56

Figure 4.6.2 $\overline{Z}_{H}$ curves for the protonation of salicylic acid..... 58

Figure 4.6.3 Speciation distribution curve for the protonation of salicylic acid plotted as a function of pH at 25 °C and 0.15 M NaCl..... 58

Figure 4.6.4 $\overline{Z}$ curves for the complexation of salicylic acid with Zr(IV)..... 59

Figure 4.6.5 $\overline{Q}$ curves for the complexation of salicylic acid with Zr(IV)..... 60

Figure 4.6.6 Speciation distribution curve of Zr(IV) complexation by salicylic acid plotted as a function of pH at 25 °C and 0.15 M NaCl..... 61

Figure 4.7.1 Structure of citric acid..... 62

Figure 4.7.2 $\overline{Z}_{H}$ curves for the protonation of citric acid..... 64

Figure 4.7.3 Speciation distribution curve for the protonation of citric acid plotted as a function of pH at 25 °C and 0.15 M NaCl at 25 °C and 0.15 M NaCl..... 65

Figure 4.7.4 $\overline{Z}$ curves for the complexation of citrate with Zr(IV)..... 66

Figure 4.7.5 $\overline{Q}$ curves for the complexation of citrate with Zr(IV)..... 67

Figure 4.7.6 Speciation distribution curve of Zr(IV) complexation by citric acid plotted as a function of pH at 25 °C and 0.15 M NaCl..... 68

Figure 4.8.1 Structure of deferoxamine..... 68

Figure 4.8.2 $\overline{Z}_{H}$ curves for the protonation of DFO-B..... 70

Figure 4.8.3 Speciation distribution curve for the protonation of DFO-B plotted as a function of pH at 25 °C and 0.15 M NaCl..... 71

Figure 4.8.4 $\overline{Z}$ curves for the complexation of DFO-B with Zr(IV)..... 72

Figure 4.8.5 $\overline{Q}$ curves for the complexation of DFO-B with Zr(IV)..... 73

Figure 4.8.6 Speciation distribution curve of Zr(IV) complexation by DFO-B plotted as a function of pH at 25 °C and 0.15 M NaCl..... 74

Figure 4.9.1 Speciation of Zr^{4+} in normal blood plasma, in the presence of DFO-B..... 75

Figure 4.9.2 Speciation of DFO-B in normal blood plasma, in the presence of Zr^{4+}..... 76

Figure 4.9.3 Blood plasma mobilization index (PMI) curves of Zr-DFO-B complex for Ca^{2+}, Mg^{2+},Cu^{2}, Cu^{2+}, Zn^{2+} and Fe^{3+}..... 77

List of Tables

Table 1.1 Decay characteristics of immuno-PET relevant radionuclides [9]. 4

Table 3.1 Composition of protonation titrations for all ligands studied..... 30

Table 3.2 Composition of metal-ligand titrations..... 31

Table 4.1 Reactions of Zr^{4+} with the most probable physiological ligands likely to disturb the Zr-DFO complex *in vivo* and their stability factors as determined by JESS.... 34

Table 4.2 Protonation constants of glutamine and equilibrium constants of Zr(IV) complexation with glutamine as determined by glass electrode potentiometry and ESTA modelling at 25 °C and ionic strength of 0.15 $mol.dm^{-3}$ NaCl..... 37

Table 4.3 Protonation constants of aspartic acid and equilibrium constants of Zr(IV) complexation with aspartic acid as determined by glass electrode potentiometry and ESTA modelling at 25 °C and ionic strength of 0.15 $mol.dm^{-3}$ NaCl..... 44

Table 4.4 Protonation constants of asparagine and equilibrium constants of Zr(IV) complexation with asparagine as determined by glass electrode potentiometry and ESTA modelling at 25 °C and ionic strength of 0.15 $mol.dm^{-3}$ NaCl..... 50

Table 4.5 Protonation constants of salicylic acid and equilibrium constants of Zr(IV) complexation with salicylic acid as determined by glass electrode potentiometry and ESTA modelling at 25 °C and ionic strength of 0.15 $mol.dm^{-3}$ NaCl..... 57

Table 4.6 Protonation constants of citric acid and equilibrium constants of Zr(IV) complexation with citric acid as determined by glass electrode potentiometry and ESTA modelling at 25 °C and ionic strength of 0.15 $mol.dm^{-3}$ NaCl..... 63

Table 4.7 Protonation constants of Desferrioxamine B (DFO-B) and equilibrium constants of Zr(IV) complexation with DFO-B as determined by glass electrode potentiometry and ESTA modelling at 25 °C and ionic strength of 0.15 $mol.dm^{-3}$ NaCl..... 69

List of Abbreviations and Symbols

ASN	Asparaginate
ASP	Aspartate
β	decay by emission of beta-particle
BFC	Bifunctional chelator
Bq	Becquerel a unit of radioactivity which is equal to one decay/s
ºC	degrees Celsius
CARST	Centre for Applied Radiation, Science and Technology
Ci	Curie a unit of radioactivity
CLI	Cerenkov Luminescence Imaging
CT	Computed Tomography
CTA	Citrate
3D	Three dimensions
Df	Desferal
DFO	Deferoxamine
E°	Electrode constant
ECCLES	Evaluation of Constituent Concentration in Large Equilibrium Systems
EGFR	Epidermal growth factor receptor
emf	Electromotive force
EOC	Epithelial Ovarian Cancer

ESTA	Equilibrium Simulation for Titration Analysis
^{18}F-FDG	[^{18}F]-Fluorodeoxyglucose
^{18}F-FLT	3'-Deoxy-3'-[^{18}F]-fluorothymidine
GLN	Glutaminate
HER2	Human Epidermal Growth Factor Receptor 2
hr	Hour
%ID/g	Injected dose per gram
JESS	Joint Expert Speciation System
keV	kilo electron volt
KHP	Potassium hydrogen phthalate
L	Ligand
LFER	Linear Free Energy Relationship
log β	logarithm of the overall formation constant
log K	logarithm of the stepwise formation constant
M	metal ion / mol.dm^3
mAbs	Monoclonal antibodies
m.b.e.	Mass-balance equation
MeV	Mega electron volt
mm	Millimetres
$\bar{n}$	Deprotonation of the free ligand
Necsa	South African Nuclear Energy Corporation SOC Ltd

pA	negative logarithm of free deprotonated ligand concentration
PET	Positron Emission Tomography
pH	negative logarithm of the free acid concentration
$\overline{Q}$	Deprotonation function (the average number of protons released on complexation per metal-ion)
R	Gas constant
ROIs	Regions of interest
SAL	Salicylate
SEER	Surveillance Epidemiology and End Results
SPECT	Single Photon Emission Computed Tomography
T	Temperature
VEGF	Vascular Endothelial Growth Factor
VEGFR	Vascular Endothelial Growth Factor Receptor
$\overline{Z}$	Complex-formation constant
$\overline{Z}_H$	Protonation function (the average number of protons bounds per ligand)

CHAPTER 1: INTRODUCTION

1.1 ZIRCONIUM

Zirconium (Zr) was first discovered in 1789 as zircon in the form of the orthosilicate and then identified as a metal in 1824 by Berzelius [1]. After its discovery, Zr was only used in the impure form of zircon, in industrial applications such as the fabrication of fake diamonds [1]. At the time, Zr received very little attention in the medical field. However, Zr was later found to have an isotope, ^{89}Zr, which belongs to a family of radiometals that produce emissions that can be harnessed for diagnostic imaging. This particular radioisotope is being utilized in positron emission tomography (PET), a modality that harnesses emissions from radioisotopes with positron emission capability. The counterparts of PET include single photon emission computed tomography (SPECT) and therapeutic applications which are limited to radiometals with particular decay capabilities. For example, SPECT utilizes radiometals such as galium-67, technetium-99m, indium-111, and lutetium-177 which produce gamma rays. Therapeutic applications on the other hand utilize radiometals such as scandium-47, yittrium-90, bismuth-212, bismuth-213, lead-212, actinium-225, rhenium-186 and rhenium-188 for procedures such as brachytherapy [2].

Radiometals have been used in the medical field for decades now and their introduction has meant that their chemical properties had to be known in detail, because the ions of each radiometal ion have unique aqueous coordination properties. However, since all the isotopes of a given element behave chemically in a similar way, it is possible to perform investigations of a particular radiometal safely and with ease using one of the stable isotopes. For example, a useful radiometal may be from an element that has multiple radioactive isotopes as well as stable isotopes. This means that it is possible to investigate a radioisotope of an element such as Zr (e.g. ^{89}Zr) using its stable isotope (e.g. ^{90}Zr). This strategy provides the same charge and chemical properties, and therefore the same biological behaviour and distribution in vivo thus ensuring easy and cost effective experimental procedures [3].

In addition, a radiometal also has to be bound to a substance called a chelator to be able to fulfil its purpose in vivo. This combination forms a ligand system that binds the radiometal ion in a tight stable coordination complex to avoid transchelation and hydrolysis [3]. Without this system, a radiometal would simply behave as it would when it is a “free metal ion” and as a result, a radiometal from an element such as Zr, which is a bone seeker, would directly accumulate in

bone [4]. The radiometal-chelate complex is further attached to a targeting moiety that helps ensure the delivery of the radiopharmaceutical to the part of the body being targeted.

1.2 IMMUNO-PET

In recent years, antibodies have gradually become the preferred targeting moiety for cancer therapy [4]. This has led to an associated rise in the development of antibody-based imaging agents [4]. ^{89}Zr can be utilised in the antibody-based PET known as immuno-PET. This diagnostic tool employs monoclonal antibodies (mAbs) or antibody fragments as targeting vectors or moieties. Immuno-PET is the preferred modality over other modalities due to its combination of the high sensitivity and resolution of PET with the selective capability of monoclonal antibodies [5]. However, the challenge with the use of monoclonal antibodies is that they have inherently slow pharmacokinetics with reacting target uptake saturation within a period of several hours or days [6]. This requires the use of positron emitters with half lives in the order of days hence favouring the use of ^{89}Zr (t1/2 = 3.27 days).

1.2.1 Principles of Immuno-PET

Immuno-PET (as with all PET) is based on annihilation coincidence detection after labelling of the monoclonal antibodies (mAbs) or antibody fragments with a positron emitting radionuclide. The emitted positron will travel a distance of 1-3 mm depending on its energy. When the positron has lost its kinetic energy, it will combine with an electron. The two photons yielded from this annihilation process will each have energy of 511 keV, emitted simultaneously at 180° in opposite directions (Figure 1.1) [7].

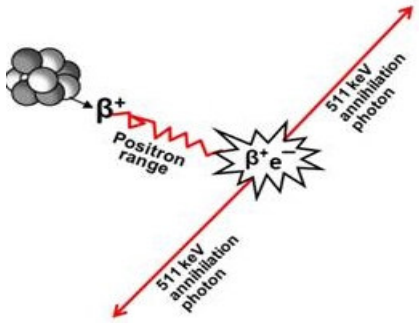

***Figure 1.1**: An illustration of positron emission and annihilation [8].*

After administering the tracer to a patient, the annihilation phenomena will allow the distribution of the compound to be monitored by coincidence detection of the photon pairs formed during

annihilation with a PET camera. A PET camera consists of detectors forming a ring around the body of the patient [9]. If the two photons are registered by detectors on opposite sides of the body differing only slightly in time of registration, it is known that somewhere along the line between the two detectors an annihilation event has taken place. This enables the formation of a 3D image. The process is illustrated in Figure 1.2 where annihilation occurs in the brain of the patient. The two photons emitted in opposite directions are detected by the detectors around the head of the patient thus allowing the location of the tumour to be deduced.

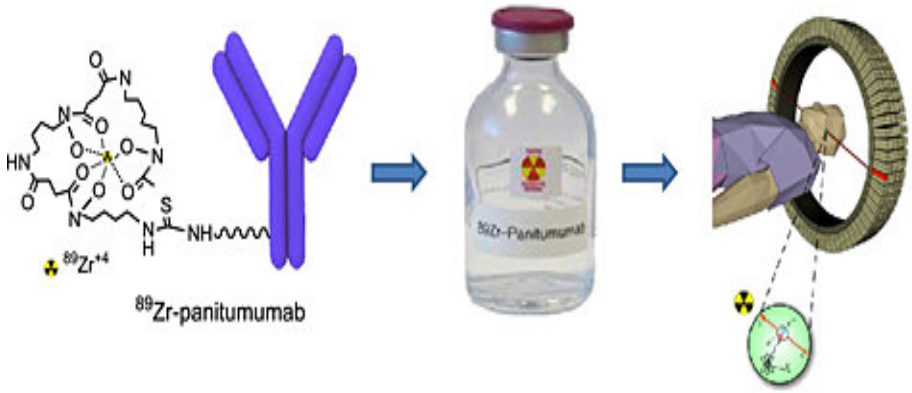

Figure 1.2: *An illustration of ^{89}Zr (IV) bound to a chelate (DFO) and attached to an antibody (Panitumumab) injected into a patient for a brain scan [10].*

1.2.2 Appropriate Radionuclides for Immuno-PET

In terms of half-lives, the positron emitter, ^{124}I (t1/2 = 101 h), is the most appropriate for the labelling of mAbs. However, most of the isotopes used for radioimmunotherapy are metals known for their tissue accumulation capabilities [6]. For example, a radiometal such as ^{89}Zr is trapped inside a target cell after the internalization of the mAb. ^{124}I on the other hand is released from the target cell after mAb internalization [11]. As a result, the use of radiometals excels and ^{89}Zr (t1/2 = 78.4 h) with a 22.7 % positron emission decay, shows more promise to be a better suited diagnostic radionuclide for quantitatively tracking the biodistribution of radiolabeled antibodies than ^{124}I. A list of some of the available radionuclides used in immuno-PET and their characteristics is given in Table 1.1.

Table 1.1: Decay characteristics of immuno-PET relevant radionuclides [9]

Isotope	Main β+ energies		Half-life	Intrinsic spatial resolution loss
	(keV)	(%)	(H)	(mm)
^{89}Zr	897	22.7	78.4	1
^{68}Ga	1899	87.9	1.13	2.3
^{18}F	634	97	1.83	0.66
^{124}I	1535	11.2	100.3	2.3
	2138	11.2		
^{64}Cu	653	17.9	12.7	0.7
^{86}Y	1221	3.01	14.7	1.8
	1545	5.6		
^{76}Br	990	5.9	16.2	5.3
	3382	5.1		
	394	27.6		
	1871	6		

^{89}Zr gives high resolution PET images due to its production of positrons with a main energy of 897 keV, which is between the main positron energies of ^{18}F (634 keV) and ^{68}Ga (1899 keV) (Table 1.1). However, although ^{18}F decays with a favourable 97 % positron emission probability and low positron energy, due to its rather short half-life (t1/2 = 1.83 h), it cannot be used for in vivo imaging of biomolecules with slow pharmacokinetics [12]. Thus, the use of ^{18}F, as well as that of ^{68}Ga (t1/2 = 1.13 h) which are the most used radionuclides in routine PET imaging procedures, is only applicable to the imaging of the biodistribution of smaller radiolabeled bioactive compounds that undergo rapid clearance from the body [12].

The limitation of short-lived nuclides to only image the biodistribution of smaller radiolabeled bioactive compounds necessitates the use of longer-lived radioisotopes for antibody-radiolabeling. This aspect opens the door for radioisotopes such as ^{124}I (t1/2 = 100.3 h) as a possible alternative for the long-term imaging. However, besides its problem with tissue accumulation, ^{124}I also has a relatively high intrinsic spatial resolution loss of 2.3 mm which is a result of its higher main positron energies, of 1535 and 2138 keV (Table 1.1). ^{89}Zr on the other hand has an intrinsic spatial resolution loss of only 1.0 mm, giving much better imaging results. Furthermore, ^{124}I does not only have a poor positron emission probability, it also produces a significant number of high-energy photons of different energies (603 keV (63.0 %), 1691 keV (10.9 %) and 723 keV (10.4 %)) which increase the background noise, while ^{89}Zr produces mainly one additional γ-line at 909 keV (909 keV (99.9 %) which is easier to deal with [11]. Therefore the application of ^{124}I increases the workload because efforts have to be made to overcome the problem with the background noise (i.e. image reconstruction techniques have to be employed) [6,12].

Other long-lived radioimmunotherapy isotopes such as; ^{64}Cu, ^{86}Y, ^{76}Br, ^{111}In, ^{67}Ga, and ^{99m}Tc with half-lives of 12.70 h, 14.70 h, 16.20 h, 2.80 days, 3.26 days and 6.0 h respectively; have been used for antibody-based nuclear imaging [3,4,13]. However, each of these isotopes possesses a feature that limits their clinical suitability. For example, despite the success of using ^{64}Cu radiolabeled antibodies in numerous pre-clinical studies on rodents, it is unsuccessful in imaging humans because its half-life (t1/2 = 2.70 h) is too short to prove effective [9]. Likewise, ^{86}Y and ^{76}Br also possess half-lives that are too short for human imaging. The main problem with isotopes with short half-lives is that to perform the production and following purification protocols in time is difficult if not impossible [4,9].

^{111}In and ^{67}Ga on the other hand possess reasonably longer half-lives, sufficient for human imaging, but these two are limited to immuno-SPECT. As a result, ^{111}In and ^{67}Ga are subject to the limitations of SPECT which is inferior to PET [14]. Furthermore, ^{99m}Tc combines the limitations of SPECT imaging with a half-life that is even shorter than that of ^{86}Y and ^{76}Br.

Eventhough ^{89}Zr has these advantages over other radioimmunotherapy isotopes, measures have to be taken regarding its transport and use because it emits very high energy photons (897 keV) which are highly penetrating. The penetrating strength of these photons requires a half-value layer of about 10mm lead [4].

1.3 CHELATORS

The labelling of antibodies with radiometals requires the use of chelators to form stable complexes. These molecules have several atoms that can form bonds to a single metal ion. Studies have shown that when attaching a targeting moiety, such as an antibody to a radiometal, bifuctional chelators are preferred. Bifuctional chelators have reactive functional groups that can be covalently attached to the antibodies [15].

Desferal (Df), the methanesulfonate salt of desferrioxamine, has proven to be the best choice as a bifunctional chelator (BFC) for tri- or tetravalent radiometal ions. It is an iron chelating agent with an amino group used for coupling to the antibodies [4]. Its metal binding moiety is formed by three hydroxamate groups, and because Zr(IV) is known to form very stable metal-hydroxamate complexes, and Df has three hydroxamate groups, Df is the chelate of choice for complexating ^{89}Zr [6]. It is expected that this complex is even more stable than the iron-Df complex, which has a log *K* of 30 [16].

1.4 STRUCTURE OF A RADIOMETAL-BASED PET TRACER

A radiometal-based PET tracer consists of three parts; the radiometal (i.e. PET-nuclide), which changes the radioactive emission properties and half-life; the chelator (i.e. linker), which must be carefully matched with the radiometal for optimal stability; and the targeting moiety (i.e. vehicle molecule), which allows for the selection of any known molecular target for site-specific delivery of the radioactive agent (Figure 1.3).

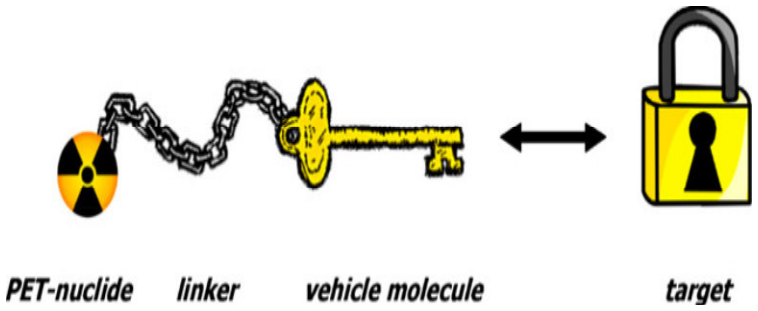

Figure 1.3: *The structure of a radiometal-based PET tracer [17].*

1.5 BENEFITS OF IMMUNO-PET

Immuno-PET has the useful ability of allowing specific uptake of molecular biomarkers. This ability makes it possible for antibodies to be able to selectively target tumour associated antigens, such as the Epidermal Growth Factor Receptor (EGFR) and the Human Epidermal

Growth Factor Receptor 2 (HER2). For example, ^{89}Zr-labeled anti- HER2 antibodies can distinguish the HER2− and HER2+ tumours and also show the intratumoral and intertumoral heterogeneity (Figure 1.4) [18]. Immuno-PET therefore makes it possible to distinguish between patients who are likely to have success from a particular therapy based on the expression of their tumour associated antigen.

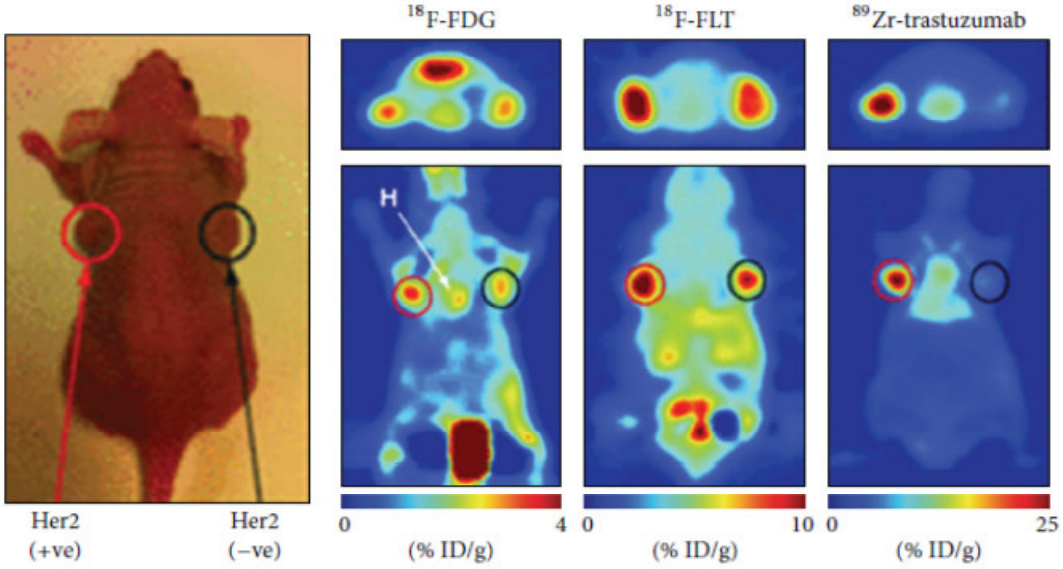

Figure 1.4: *An illustration of the distinguishing capability of immuno-PET regarding the HER2− and HER2+ tumours in a tumour bearing mice [18].*

The images show ROIs (%ID/g) for ^{89}Zr-trastuzumab, ^{18}F-FDG, and ^{18}F-FLT of athymic nude mice bearing HER2+ and HER2− MKN-74 With respect to ^{89}Zr, the images (Figure 1.4) shows that the ^{89}Zr-labelled antibody produces higher quality images with reduced background (i.e. the image formed with the ^{89}Zr-labelled antibodies shows the absence of the HER2− tumour clearer than its counterparts).

The use of immuno-PET is preferred over immuno-SPECT since it produces images with better spatial resolution. This attribute allows images to be analyzed quantitatively more accurately. This technique also differs from other conventional imaging modalities such as ultrasonography, radiography and computed tomography (CT) which only offer static images thus making it superior by its ability to form functional images. Furthermore, PET is also considered the most specific and accurate method for tumour localization and has allowed significant improvements in radiation dose estimation [11].

1.6 ^{89}Zr-LABELED ANTIBODIES IN CANCER THERAPY

At present, ^{89}Zr-labeled antibodies directed against different tumour associated antigens are tested in pre-clinical studies. These antigens include the Vascular Endothelial Growth Factor (VEGF), EGFR and HER2 [15]. VEGF is a proangiogenic factor in both tumours and normal tissues. The overexpression of this antigen and its receptors is often associated with poor prognosis [19]. The interest in EGFR on the other hand comes from the fact that it is a member of the ErbB family. The ErbB family is a family of receptors that play a part in propagating signals regulating cell differentiation, apoptosis proliferation and motility [15]. EGFR is expressed in a variety of human tumours, including carcinomas and gliomas of the lung, breast, colon, kidney, bladder, and ovary [20]. The overexpression of the EGFR antigen is associated with more aggressive tumours and poor prognosis. HER2 also belongs to the ErbB family. It plays a part in differentiation, angiogenesis, proliferation, metastasis, and cell survival upon heterodimerization with other members of the EGFR family and its overexpression is found in tumours such as breast and ovarian cancer [21].

1.7 EPITHELIAL OVARIAN CANCER (EOC)

The ability of ^{89}Zr-labeled antibodies to target tumour associated antigens (VEGF, EGFR and the HER2) means that this approach has the potential of providing a breakthrough in overcoming cancers such as epithelial ovarian cancer, which is associated with the EGFR expression [18]. Despite its relative rarity in the general population and the availability of standard treatment through surgical intervention and platinum chemotherapy, epithelial ovarian cancer continues to be one of the most problematic forms of cancer affecting women in the western world. The Surveillance Epidemiology and End Results (SEER) program estimated that 21,980 new cases of ovarian cancer occur in 2014, with 14,270 deaths resulting from this disease in the United States of America alone [22].

Patients with this form of cancer often present the disease at an advanced stage and due to its associated poor prognosis as well as the chances of developing resistance to conventional chemotherapy during the course of treatment; the result is a poor 30 % 5-year survival rate [23]. To improve ovarian cancer prognosis, there is a clear need for additional therapeutic options. However, with the use of ^{89}Zr-labeled antibodies, certain humanized monoclonal antibodies (mAbs) have been found which can treat ovarian cancer through targeting the EGFR over expression [24].

Furthermore, ^{89}Zr-labeled antibodies have not only made their breakthrough into pre-clinical studies, they have also made their mark in clinical studies. The first immuno-PET human trial

can be traced back to more than ten years ago at the VUmc in Amsterdam, an investigation involving ^{89}Zr-labeled-cmAb U36 [25]. Following this trial, a number of other clinical Immuno-PET trials were conducted at other institutions in different countries including the Jules Bordet Institute in Belgium where research involving ^{89}Zr-labeled rituximab was carried out. The researchers at Jules Bordet Institute conducted their study with the aim of comparing the diagnostic accuracy of ^{89}Zr-rituximab-PET/CT with standard [^{18}F] FDG-PET/CT in patients with CD20+ B-cell lymphoma [26]. After obtaining perfect images from ^{89}Zr-rituximab-PET/CT, it was established that the ^{89}Zr-labeled rituximab is effective in quantification of CD20 antigen expression [27]. It can also be seen that immuno-PET/CT with ^{89}Zr-rituximab (Figure 1.5) shows a reduced background compared to [^{18}F] FDG-PET/CT.

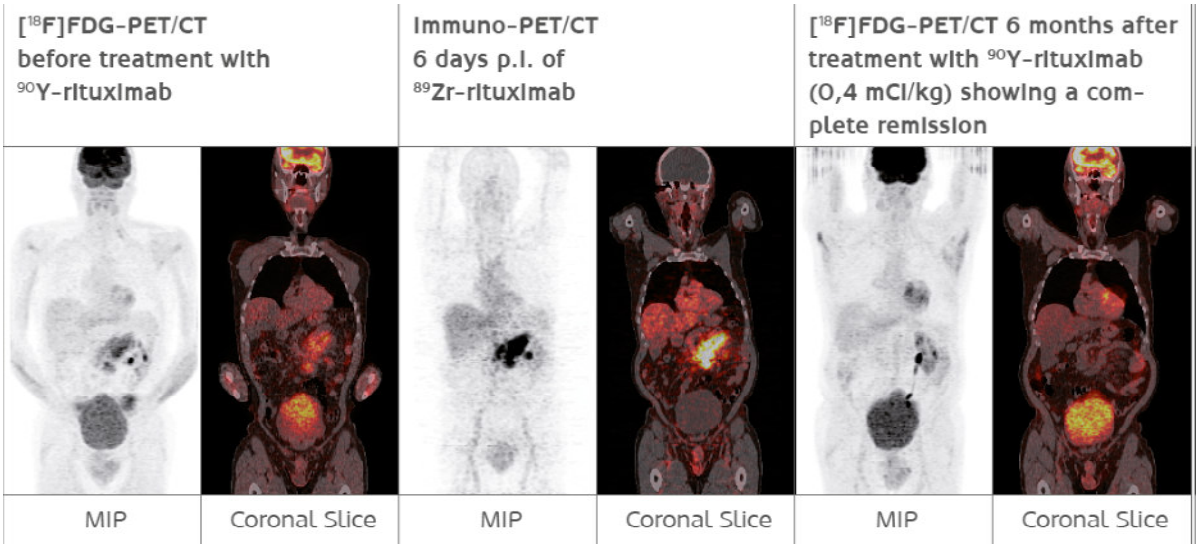

Figure 1.5: *Images obtained from an immuno-PET/CT imaging study conducted at Jules Bordet Institute, comparing ^{89}Zr-rituximab with [18F] FDG-PET/CT in a patient with CD20+ Bcell lymphoma [26].*

1.8 OTHER MEDICAL APPLICATIONS

The use of ^{89}Zr is not only limited to PET alone; this radioisotope is also used in Cerenkov Luminescence Imaging (CLI), an imaging modality based on a phenomenon that results in optical photons being emitted when a charged particle travels at a speed greater than that of light in a medium [28]. It is a fully quantifiable technique and can be correlated to the respective

PET signal. ^{89}Zr-labeled antibodies are used in an application of CLI known as image-guided surgery. However, ^{89}Zr is best suited for PET and for this reason its application will remain in vivo PET imaging of biological processes [28].

1.9 QUALITY CONTROL

Generally the use of radiopharmaceuticals is subject to laws that pertain to the use of all drugs which suggest that a series of regulatory and legal aspects have to be followed prior to human release. Since these parenterals are administered intravenously, stricter regulations have to be in place to account for every material associated with their use (i.e. glass tubes, rubber materials for stoppers and sterility assessment). Even the short half-life of PET radionuclides does not make these tasks easier. However, in the case of ^{89}Zr, there is a specially made system that ensures its safe and routine production, thus making the radioisotope easy to work with. This custom-made system produces a radionuclidic purity of almost a 100% [29].

1.10 RESEARCH OBJECTIVE

The primary objective of this research was to promote the understanding of ^{89}Zr as an imaging radioisotope used in cancer diagnosis. The purpose is to determine the possibility that exists of the in vivo release of the imaging agent. The agent may dissociate and interact with ions and plasma ligands which are present in high concentrations within the blood plasma.

The aim was therefore to understand the speciation of the ^{89}Zr metal ion and its ligand of choice, deferoxamine (DFO). The speciation of these two chemical substances can depict their behaviour in vivo by describing the composition and concentration of every species in the chemical sample they are in. The use of speciation can determine the toxicity, biodistribution and excretion of an element. However, in dynamic systems such as blood plasma, determining the speciation of a particular element is often hard to achieve. Therefore, powerful computer modelling programs such as JESS (Joint Expert Speciation System), ESTA (Equilibrium Simulation by Titration Analysis) and ECCLES (Evaluation of Constituent Concentrations in Large Equilibrium Systems) are used.

In order to understand the speciation of the ^{89}Zr(IV) metal ion, it was therefore necessary to determine the stability of the ^{89}Zr-DFO complex in the presence of ^{89}Zr(IV) susceptible blood plasma ligands as extracted by the JESS computer program. These ligands were then evaluated using the ECCLES computer program, modelling the in vivo behaviour thus establishing the ^{89}Zr blood plasma model. This was achieved by studying the protonation of the physiological ligands (citrate, glutaminate, aspartate, asparaginate and salicylate (Figure 1.6))

which were found to show affinity for Zr(IV), together with DFO. Their complexation behaviour with Zr(IV) was studied through the use of glass electrode potentiometry (GEP).

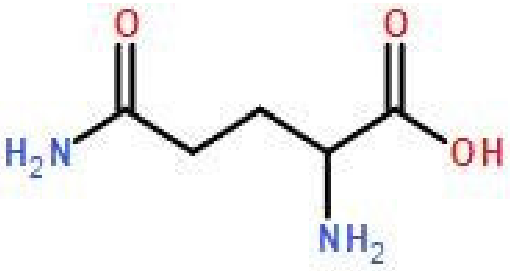

glutamine

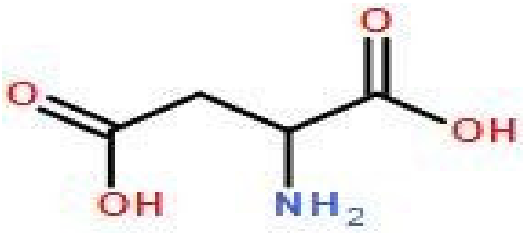

aspartic acid

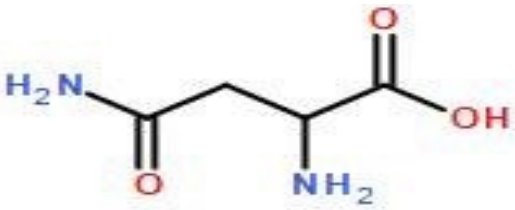

Asparagine

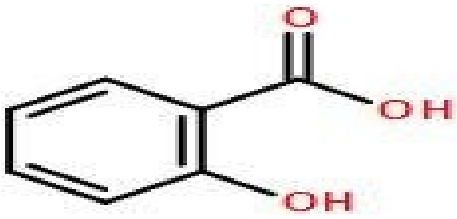

salicylic acid

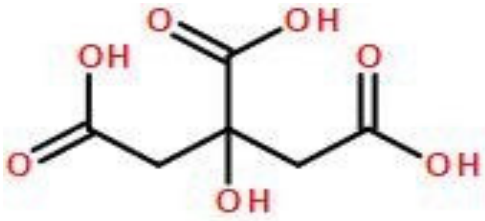

citric acid

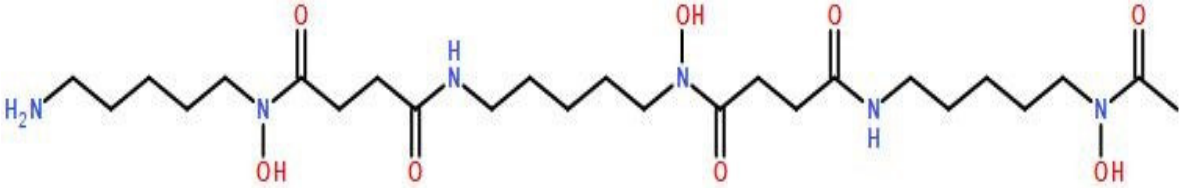

DFO

***Figure 1.6**: Structures of the ligands studied with Zr(IV)*

The data obtained from potentiometric experiments was processed by a computer package of programs known as ESTA for the optimization of data and refinement of protonation and formation constants. These formation constants were then used in the simulation of binding interactions of *in vivo* ligands using ECCLES thus developing the blood plasma model for Zr(IV). Once the blood plasma model was determined, it was determined whether the potential competitive blood plasma ligands that are likely to disturb the ^{89}Zr-DFO complex would be successful. The experimental work in this thesis was performed with stable Zr(IV), which served to simulate the behaviour of ^{89}Zr(IV) due to their similar chemical properties.

1.11 THESIS OUTLINE

In Chapter 1 the basic information about the ^{89}Zr radiometal, immuno-PET, and the significance of immuno-PET in the treatment of epithelial ovarian cancer is discussed. This chapter aims to show ^{89}Zr as the future radionuclide for immuno-PET with a better success of bringing the battle against the horror of epithelial ovarian cancer to an end. It starts by giving the background of Zr and why it is considered to be ‘‘the next best thing’’ in PET tracers by comparing it to available radiotracers. An explanation of how PET works is given with a further explanation of how immuno-PET with ^{89}Zr can treat epithelial ovarian cancer. The aims and objectives of this research project are also outlined in this chapter.

Chapter 2 is the literature review describing the theoretical background of the most applicable experiments to produce the data required for this research. It gives the understanding of how the results from the in vitro studies can be translated to a biological system. Potentiometry, ESTA and ECCLES, which are useful in the establishment of the blood plasma model, are also explained.

Chapter 3 is the methodology, where research design, methods, procedures and processes of data collection and analysis are explained.

Chapter 4 includes data presentation, analysis and discussion.

Chapter 5 concludes on whether the aims and objectives have been achieved.

REFERENCES

[1] Abou DS, Ku T, Smith-Jones PM. In vivo biodistribution and accumulation of ^{89}Zr in mice. Nucl Med Bio 2011;38:675-681.

[2] World Nuclear Association. Radioisotopes in Medicine. 2015. http://www.world-nuclear.org/information-library/non-power-nuclear-applications/radioisotopes-research/radioisotopes-in-medicine.aspx [Accessed on 28 Sep 2015].

[3] Price EW, Orvig C. Matching chelators to radiometals for radiopharmaceuticals. Chem Soc Rev 2014;43:260.

[4] Deri MA, Zeglis BM, Francesconi LC, Lewis JS. PET imaging with ^{89}Zr: From radiochemistry to the clinic. Nucl Med Bio 2013;40:3-14.

[5] Zbar AP, Guillou PJ, Bland KI, Syrigos KN. Immunology for Surgeons. Springer Science & Business Media, 2012, p, 368.

[6] Meijs WE, Haisma HJ, Klok RP, van Gog FB, Kievit E, Pinedo HM, et al. Zirconium-labeled monoclonal antibodies and their distribution in tumor- bearing nude mice. J Nucl Med 1997;38:112-118.

[7] Verel I, Visser GW, van Dongen GA. The promise of Immuno-PET in radioimmunotherapy. J Nucl Med 2005;46:164S-71S.

[8] Velikyan I. Prospective of ^{68}Ga-radiopharmaceutical development. Theranostics 2014;4:47-80.

[9] Reddy S, Robinson MK. Immuno-Positron Emission Tomography in cancer models. Semin Nucl Med 2010;40:182-189.

[10] Wei L, Shi J, Afari G, Bhattacharyya S. Preparation of clinical-grade ^{89}Zr-panitumumab as a positron emission tomography biomarker for evaluating epidermal growth factor receptor-targeted therapy. J Labelled Comp Radiopharms 2013;57:25-35.

[11] Vosjan M, Perk LR, Rispens SI. ^{89}Zr-Immuno-PET: Physical properties, production, labeling and applications of ^{89}Zr. http://www.cyclotron.nl/10_3_1 [Accessed on 3 Dec 2015].

[12] Fischer G, Seibold U, Schirrmacher R, Wängler B, Wängler C. ^{89}Zr, a radiometal nuclide with high potential for molecular imaging with PET: chemistry, applications and remaining challenges. Molecules 2013;18:6469-6490.

[13] Perk LR, Vosjan MJWD, Visser GWM, Budde M, Jurek P, Kiefer GE, et al. *P-Isothiocyanatobenzyl-desferrioxamine*: a new bifuctional chelate for facile radiolabeling of

monoclonal antibodies with zirconium-89 for Immuno-PET imaging. Eur J Nucl Med Mol Imaging 2010;27:250-259.

[14] Holland JP, Divilov V, Bander NH, Smith-Jones PM, Larson SM, Lewis JS. ^{89}Zr-DFO-J591 for ImmunoPET of prostate-specific membrane antigen expression in vivo. J Nucl Med 2010;51:1293–1300.

[15] Zhang Y, Hong H, Cai W. PET tracers based on zirconium-89. Current Radiopharms 2011;4:131-139.

[16] Meijs WE, Herscheid JDM, Haisma HJ, Pinedo HM. Evaluation of desferal as a bifuctional chelating agent for labelling antibodies with ^{89}Zr. Appl Rod & Isor 1992;43:1443-1444.

[17] Wadsak W, Mitterhauser M. Basics and principles of radiopharmaceuticals for PET/CT. Eur J Rad 2010;73:461-469.

[18] Holland JP, Caldas-Lopes E, Divilov V, Longo VA, Taldone T, Zatorska D, et al. Measuring the pharmacodynamic effects of a novel Hsp90 inhibitor on HER2/neu expression in mice using ^{89}Zr -DFO-Trastuzumab. PLoS ONE 5: e8859.

[19] Padro T, Bieker R, Ruiz S, Steins M, Retzlaff S, Bürger H, et al. Overexpression of vascular endothelial growth factor (VEGF) and its cellular receptor KDR (VEGFR-2) in the bone marrow of patients with acute myeloid leukemia. Leukemia 2002;16:1302-1310.

[20] Krasindskas AM. EGFR Signalling in colorectal carcinoma. Pathology Res Int, Article ID. 32932, 2011.

[21] van de Watering FCJ, Rijpkema M, Perk L, Brinkmann U, Oyen WJ, Boerman OC. Zirconium-89 labelled antibodies: A new tool for molecular imaging in cancer patients. BioMed Res Int 2014:5-6.

[22] Sharma SK, Wuest M, Wang M, Glubrecht D, Andrais B, Lapi SE, et al. Immuno-PET of epithelial ovarian cancer: harnessing the potential of CA125 for non-invasive imaging. EJNMMI Res 2014;4:60.

[23] van der Bilt AR, Terwisscha van Scheltinga AG, Timmer-Bosscha H, Shröder CP, Pot L, Kosterink JG, et al. Measurement of tumor VEGF-A levels with ^{89}Zr-Bevacizumab PET as an early biomarker for the antiangiogenic effect of Everolimus treatment in an ovarian cancer xenograft model. Clin Cancer Res 2012;18;6306.

[24] Prof Dr Zeevaart JR. Personal communication.

[25] Börjesson PK, Jauw YW, de Bree R, Roos JC, Castelijns JA, Leemans CR, et al. Radiation dosimetry of zirconium-89-labeled chimeric monoclonal antibody U36 as used for Immuno-PET in head and neck cancer patients. J Nucl Med 2009;50:1828.

[26] Muylle K. Immuno-PET imaging with -PET imaging with ^{89}Zr-rituximab rituximab in CD20+ B-cell lymphoma. Jules Bordet Cancer Inst, Belgium 2011.

[27]. Perk L, Rispens SI. The future of Immuno-PET in drug development: zirconium-89 and iodine-124 as key factors in molecular imaging. http://www1.cyclotron.nl/library/resource/file/pdf/cyclotron_101008_fin_korr_low.pdf [Accessed on 13 Oct 2015]

[28] Li C, Mitchell GS, Cherry SR. Cerenkov luminescence tomography for small-animal imaging. Optics Letters 2010;35:1109-1111.

[29] Wooten AL, Madrid E, Schweitzer G. Routine production of ^{89}Zr using an automated module. Appl Sci 2013;3:593–613.

CHAPTER 2: THEORETICAL BACKGROUND

2.1 INTRODUCTION

In the study of metal ion coordination equilibria in biological systems, metal-exchange competition experiments are the most applicable. These experiments provide a direct measure of the stability by competition with the most likely transchelation ligands in vivo [1]. The stability is directly determined from the formation constants which are simply equilibrium constants for the formation of the radiometal complex in solution. These constants are the measure of the strength of a complex formed when a radiometal and chelate come together. The formation constants simply provide the information required to calculate the concentration of the complex in solution [2].

However, the thermodynamic data of metal ion-ligand complex formation provide significant information. Their constants are determined by the thermodynamic equilibrium constant, *K*.

For the equilibrium (where M = metal-ion and L = ligand)

$$M + L \rightleftharpoons ML \tag{2.1.1}$$

the thermodynamic equilibrium can be defined as

$$K = \frac{\{ML\}}{\{M\}\{L\}} \tag{2.1.2}$$

where {ML} = activity of the chemical species ML.

Taking into consideration that complex formation often occurs in steps, one ligand being added in each step, the overall formation constant can be described as the product of the step-wise formation constants. As the complex becomes more stable, the formation constant becomes larger.

$$\beta_n = K_1K_2K_3\ldots K_n = \prod_{i=1}^{i=n} K_i \tag{2.1.3}$$

For the reaction

$$aM + bL + cH \rightleftharpoons M_aL_bH_c \quad (2.1.4)$$

The formation constants can be represented as follows

$$\beta_n = \frac{[M_aL_bH_c]}{[M]^a[L]^b[H]^c} \times \Gamma \quad (2.1.5)$$

(Where M = metal ion, L = ligand, H = hydrogen ions within a complex, Γ = quotient of activity coefficients and a, b, c = number of moles of each chemical specie) [3].

The formation constants are usually experimentally determined by potentiometric and/or spectrophotometric titrations. Potentiometry is probably the oldest and most extensively used because of the easy availability of the electrodes, high sensitivity and reproducibility of experimental results, making it the most precise and accurate non-invasive technique available at present [4].

2.2 POTENTIOMETRY

Potentiometry is based on the interpretation of electrode potentials generated by the chemical interaction between acids (metal ions) and bases (ligands) [5]. This titration technique does not require the use of an indicator but instead the potential is measured across the analyte [6].

The potential is measured by the indicator electrode (the glass electrode and metal ion indicator electrode) and a reference electrode. Silver chloride electrodes are often used as reference electrodes. The reference electrodes basically function as redox electrodes, and in the case of silver chloride electrodes, the reaction occurs between the silver metal and its salt [7].

The reactions can be presented as follows:

$$Ag^+ + e^- \rightleftharpoons Ag(s) \quad (2.2.1)$$

$$AgCl(s) \rightleftharpoons Ag^+ + Cl \quad (2.2.2)$$

Or an overall reaction can be written:

$$AgCl(s) + e^- \rightleftharpoons Ag(s) + Cl^- \quad (2.2.3)$$

This is a very efficient reaction, characterized by fast electrode kinetics, which occurs according to these equations in solutions of pH values between 0 and 13.5.

The indicator electrode on the other hand forms an electrochemical half cell comprising of ions of interest present in the solution. The corresponding equation can be presented as follows;

$$Zr^{4+} + 4e^- \rightleftharpoons Zr(s) \quad (2.2.4)$$

The overall electric potential is calculated as

$$E_{cell} = E_{ind} - E_{ref} + E_{sol} \quad (2.2.5)$$

where E_{sol} = potential difference over the test solution between the two electrodes, E_{ind} = potential at the indicator electrode, E_{ref} = potential at the reference electrode and E_{cell} = potential recorded at intervals as the titrant is added [8].

E_{cell} depends on the concentration of the relevant ions which the indicator electrode is in contact with. For example, the electrode reaction may be

$$M^{n+} + ne^- \rightleftharpoons M \quad (2.2.6)$$

A change in concentration of M^{n+} would be accompanied by a corresponding change in the E_{cell}. This relationship is the basis of the potentiometric titration which measures the E_{cell} with addition of titrant [7].

The equilibrium reduction potential of a half cell in an electrochemical cell can be determined by the Nernst equation. This equation relates the E_{cell} to the standard potential and to the activities of the electroactive species. The electrode potential of a half reaction can be calculated from the concentrations of the individual species comprising the process, as well as the conditions such as temperature. For the reaction

$$aA + bB + \ldots ne^- \rightleftharpoons cC + dD \quad (2.2.7)$$

where A, B, C, D = molecular species, e^- = electron, and the lower case a, b, c, d = number of moles of each species taking part in the given half cell reaction. The electrode potential *E* for this reaction can be written as

$$E = E^0 - \frac{RT}{nF} \ln \frac{\{C\}^c \{D\}^d}{\{A\}^a \{B\}^b} \quad (2.2.8)$$

where E° = standard electrode potential [9]. The Nernst equation is more commonly written in base 10 log form and substituting the constants R = 8.314 JK^{-1}, T = 298 K, F = 96485 C/mol, the equation becomes:

$$E = E^0 - \frac{0.0592}{n} \log \frac{\{C\}^c \{D\}^d}{\{A\}^a \{B\}^b} \quad (2.2.9)$$

2.3 GLASS ELECTRODE POTENTIOMETRY (GEP)

Glass electrode potentiometry (GEP) is effective in this study (i.e. determination of formation constants) because of its ability to show rapid reversibility, linear Nernst equation response, and high sensitivity to aqueous hydrogen ions over a wide concentration range [4]. This is a well established electro-metric titration technique for the determination of complex stability constants of a ligand in the presence or absence of metal ions in complex speciation measurements [10]. With this technique, the labile equilibrium existing between metal ions, ligands and protons is not affected.

The GEP measuring setup for potentiometric measurements always consist of two electrodes, a measuring or indicator electrode and a reference electrode. These two electrodes are usually contained in a single combined glass electrode for practical reasons as illustrated in Figure 2.1.

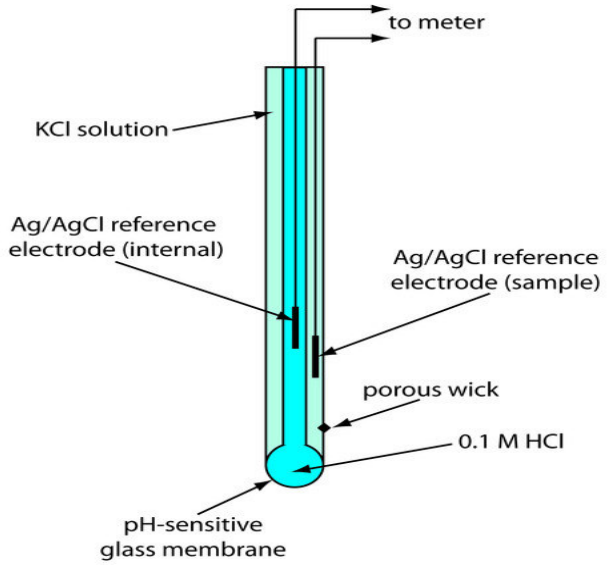

Figure 2.1: *An illustration of a typical glass electrode used for measuring pH [7].*

2.4 MODELLING

Potentiometry can be used as a method for determining the formation constants through processing the potentiometric data with computer software programs such as ESTA (Equilibrium Simulation for Titration Analysis). ESTA is a sophisticated and complex speciation computer program that can effectively analyze potentiometric titration data and simulate the equilibrium distributions of chemical species [11]. This program solves the mass-balance equations by equating the experimental concentrations (T_i^r) with the calculated total concentrations (T_i^c) [5,10].

$$T_i^r = T_i^c \text{ , I =1… NC} \qquad \text{for NC complexes} \tag{2.4.1}$$

$$\text{Where} \quad T_i^c = [X_i] + \sum_{J=1}^{NJ} r_{ji} \Gamma_j \beta_j \prod_{n=1}^{NC} [X_n]^{rjn} \tag{2.4.2}$$

$$T_i^r = \frac{C_i^v V^\circ + \sum_{m=1}^{NB} C_{im}^B \nu_m}{V^\circ + \sum_{m=1}^{NB} \nu_m} \quad (2.4.3)$$

$$\Gamma = \left(\prod_{n=1}^{NC} \gamma_n^{rjn} \right) \Big/ \gamma_j \quad (2.4.4)$$

where:

$[X_i]$ = free concentration of the i^{th} component

r_{jn} = stoichiometric coefficient of component *i* in complex j

NJ = number of complexes

NC = number of concentrations

C_i^V = initial concentration of the i^{th} component in the vessel

C_{im}^B = concentration of the i^{th} component in the m^{th} burette

V_m = total titre volume added from m^{th} burette

V° = initial vessel volume

NB = number of burettes

γ_n = activity coefficient of species n

γ_j = activity coefficient of species j

These equations are solved by calculating for “NC-free” concentrations, where the electrode equation is evaluated for free electrode ion concentrations $[X_k]$.The emf is linked to the concentration of the electrode ion by ESTA at each k^{th} titration step shown by the following equation:

$$E_k = E_k^\circ + E_k^s + E_k^j \quad (2.4.5)$$

where E_k° = electrode response intercept, E_k^s = electrode selectivity and E_k^j = liquid-junction potential. The programme also accounts for the known effects of interfering ions when using the Eisenman equation (Eq.2.4.6) by correcting changes of the liquid-junction potential, E_k^j, when the glass electrode is calibrated;

$$E_k^j = -\frac{RT}{F} In\left(1 + d\frac{[X_H]}{I}\right) \quad (2.4.6)$$

where I = concentration of the background univalent electrolyte.

Potentials differences across junctions of different univalent electrolytes can be predicted by the Henderson equation at constant ionic strength. The equation is applicable at pH smaller than 2 where the liquid junction potential becomes significant. Parameters such as formation constants, electrode response intercept, and the unknown free concentrations can be calculated from other parameters that are determined experimentally or derived from the electrode equations.

In ESTA, Gauss-Newton algorithms are used to optimize a calculated model representation of the experimental data. The experimental parameters such as formation constants and initial concentrations are calculated first, at the first and second titration points from experimental values [5]. The $[X_k]$ can be calculated from these initial estimates and their respective electrode potentials. This program simulates the experimental titration data to optimize a favourable representation of the formation of complexes within the solution [12]. A satisfactory model is assumed when there is a close fit between the calculated parameters and the experimental data as well as a small standard deviation of the parameters and Hamilton R-factor. The Hamilton R-factor gives an indication of the difference of the objective function that has been minimized and the experimental data points [9].

The ESTA library contains two main program modules which perform different calculations, namely, ESTA1 (simulation mode) and ESTA2 (optimization mode). The programs account for associated changes in activity coefficients and variations of ionic strength [13].

2.4.1 ESTA1: the simulation mode

This program produces results on a point by point basis, single values for any titration parameter which includes formation constant estimates, emf values and initial vessel

concentration. It can also calculate the distribution of species taking part in an equilibrium system as a function of pH. The programs used to generate formation functions are [5]:

- $\overline{Z}_H$ and $\overline{n}$ (protonation functions), the number of protons bound by the free ligand in the absence of complexation at a certain pH.

$$\overline{Z}_H = \frac{(T_H - H + OH)}{T_{Lig}} \tag{2.4.1.1}$$

Where T_H = total hydrogen concentration, T_{Lig} = the total ligand concentration and OH = concentration of the hydroxide ions.

For binary systems a formation function is defined for the ligand subsystem.

$$\overline{n} = \frac{\left(T_H^* - H + OH\right)}{T_L^r} \tag{2.4.1.2}$$

- $\overline{Z}$ (complex-formation constant), the number of ligands bound per metal-ion(s) at a certain pH.

$$\overline{Z} = \frac{T_L - A\left(1 + \sum_n \beta_{LHn} H^n\right)}{T} \tag{2.4.1.3}$$

Where A = the protonation function divided by $\left(\sum_n n\beta_{LHn} H^n\right)$ and T is the total metal ion concentration

- $\overline{Q}$ (deprotonation function), the number of protons released by the ligand during the formation of a complex at a certain pH.

$$\overline{Q} = \frac{\left(T_H^* - T_H\right)}{T_M} \tag{2.4.1.4}$$

Where T_H^* is the calculated total concentration of protons of the system at certain pH.

This program can be used to draw graphs of $\overline{Z}$ *vs* pA and pH *vs* $\overline{Z}_H$ or $\overline{Q}$.

2.4.2 ESTA2: the optimization modules

There are two optimizing programs within ESTA2, namely ESTA2B and ESTA2A which differs only by the way the data are weighed. These programs can determine parameters based on a least square procedure applied to the whole system of titrations [14]. Formation constants, initial vessel volume, electrode slope, and burette concentrations can be refined with these programs. These refinements can be done by grouping any of the above mentioned parameters together as a single entity [13].

ESTA2 programs basically model the formation constants to reach low and acceptable Hamilton factors and standard deviations. Thereafter, the proposed model of formation constants can be evaluated by comparing $\overline{Q}$ and $\overline{Z}$ [10]. The sum of squares of residual may also be minimized with respect to either total concentration (OBJT) or emf task (OBJE) [13].

2.4.3 ECCLES

The ECCLES (Evaluation of Constituent Concentrations in Large Equilibrium Systems) computer software package is used to calculate the metal ions speciation and ligands in biological fluids such as blood plasma [3]. These calculations provide an indication of whether the complex of interest would be able to withstand the competition of other metal ions and ligands present in the blood plasma and if the radiometal of interest will reach targeted the area in the body [14]. In the development of a speciation model, a series of chemical equilibria representing the chemical species being investigated are generated and the equilibrium constants for the reactions have to be made distinctive.

$$S_j = \beta_j \prod_i X_i^{k(i,j)} \qquad (2.4.4.1)$$

Where S_j = concentration of species, β_j = equilibrium constant, X_i = free component concentration and k(i,j) = component stoichiometric coefficient.

From the series of equilibria and the total or free component concentrations, mass balance equations can be set.

$$T_i = X_i + \sum_j S_j k(i,j) \qquad (2.4.4.2)$$

These mass balance equations can be solved by the ECCLES computer simulation program.

REFERENCES

[1] Price EW, Orvig C. Matching chelators to radiometals for radiopharmaceuticals. Chem Soc Rev 2014;43:260.

[2] Gutten O, Rulíšek L. Predicting the stability constants of metal-ion complexes from first principles. Inorg Chem 2013;52:10347–10355.

[3] Raqhai T. Synthesis of and potentiometric studies with bisphophonate ligands APDDAM and Poly-HEDP as potential carriers of radionuclides: In attempt to develop effective ^{117m}Sn radiopharmaceuticals for bone metastases. UJ, MSc Thesis, 2012, p, 23-24.

[4] Mokalane k. Investigation of the solution chemistry and dermal absorption of novel Copper (II) chelating agents that can serve as potential anti-inflammatory drugs. UCT, MSc Thesis, 2011, p, 35.

[5] Jansen DR. An in vitro approach to evaluate and develop potential ^{117m}Sn-based bone-seeking radiopharmaceuticals. TU Delft, PhD Thesis, 2010, p, 7-15.

[6] Wang J. Potentiometry. Anal Electrochem 2006;3:165.

[7] Harvey D. Modern Analytical Chemistry, 1st Edition. Analytical Chemistry 2000:465-473.

[8] Potentiometric titrations; Location of End Points. 2015. http://www.expertsmind.com/topic/potentiometric-titrations/location-of-end-points-910938.aspx[Accesed on 13 Nov 2015].

[9] Sepini LC. A thermodynamic evaluation of 1,4,7,10-tetraazacyclododecane-1,4,7,10-tetra(methane-phosphonic acid) (DOTP) as a component of the bone-seeking radiopharmaceutical [^{177}Lu]Lu(III)-DOTP, towards establishing blood plasma model for Lu(III). NWU, MSc Thesis, 2012, p, 17-22.

[10] Liyanage JA. Chemical speciation of nickel-glycine complexation. J Sci Univ Kelaniya 2003;1:1-13.

[11] Odisitse S. Thermodynamic properties of diamino-diamide ligand as potential anti-flammatory agent. UCT, MSc Thesis, 2003, p, 29.

[12] Gabanamotse K. The complexation of selected blood plasma ligands with Sn(IV) used to predict the in vivo behaviour of Sn(IV)-PEI-MP. NWU, MSc Thesis, 2007, p, 37.

[13] K. Murray and P. M. May, ESTA (Equilibrium Simulation for Titration Analysis) Manual, University of Wales Institute of Science and Technology, Cardiff, 1984.

[14] Zeevaart JR. Metal-ion speciation in blood plasma as a tool in predicting the *in vivo* behaviour of potential bone-seeking radiopharmaceuticals. TU Delft, PhD Thesis, 2001, p, 10-13.

CHAPTER 3: EXPERIMENTAL

3.1 REAGENTS

All reagents were of analytical grade: hydrochloric acid (HCl, F.W. 36.46, 32 % pure, density = 1.16 kg/l), sodium chloride (NaCl, F.W. 58.44 $g.mol^{-1}$, 99.5 %), sodium hydroxide Titrisol (NaOH, 0.1M in 500ml solution), L-asparagin (monohydrat) (F.W. 150.14) obtained from MERCK. Zirconium chloride ($ZrCl_4$, F.W. 233.02, 99.99 %), citric acid anhydrous (F.W. 192.1), L-glutamine (F.W. 146.1, 99 %), L-aspartic Acid (F.W. 138.1, 98 %) were obtained from SIGMA-ALDRICH. Salicylic acid (F.W. 138.1) was obtained from BDH Laboratory Chemicals. Desferrioxamine mesylate (F.W. 656.8) was the product of Ciba-Geigy. Demineralised water used in the preparations of solutions was prepared by passing de-ionised water through a Milli-Q-water purification system.

3.2 METHODS

3.2.1 Preparations of Solutions

A background electrolyte solution of 0.15 M NaCl was prepared by dissolving 17.532 g NaCl in de-ionised water to a total volume of 2 dm^3.

The appropriate amount 11.688 g NaCl was weighed and added into a 2 dm^3 volumetric flask to make a 0.1 M NaCl, and a solution of 0.05 M NaOH in 0.1 M NaCl (Titrisol) was added and filled to the mark.

The 0.05 M HCl in 0.1 M NaCl solution was prepared by adding 5.844 g NaCl and 4.91 ml HCl in a 1 dm^3 volumetric flask and diluting to the mark with de-ionised water.

The concentration of all the ligands used in all titrations was about 1 x 10^{-2} M. These solutions were prepared by weighing out the required amount of ligand and NaCl in a 100ml flask filling to the mark with de-ionised water. The $ZrCl_4$ used in the titrations was weighed and added directly into the reaction vessel.

A solution of 3 M KCl was prepared by weighing 22.368 g KCl, into a 100 ml volumetric flask and filling to the mark with de-ionised water.

3.2.2 Experimental Set-up

The Metrohm Titroprocessor TIM 865 jacketed vessel was used to perform all the potentiometric titrations. It was complemented by a Metrohm 665 dosimat and a model 6.0259.100 (Metrohm) combination electrode (Ag/AgCl reference) equipped with a magnetic stirrer (Figure 3.1). The dosimat was not connected to the system. It was used to add 0.15 M NaCl directly into the vessel.

Figure 3.1: *Photo of the experimental set-up used in this study.*

All titration solutions were held at a 0.15 M NaCl ionic strength to simulate blood plasma and at a temperature of 25.0 ± 0.1 ºC which was attained by circulating water around the jacketed vessel. Nitrogen gas was also passed through the solutions to create an inert atmosphere (Figure 3.2). To determine the protonation constants of the ligand, protonation titrations were performed, followed by metal-ligand titrations of which the data was used to determine formation constants. During titrations, aliquots of 0.050 ml NaOH (carbonate-free) were added in 0.10 ml NaCl to start the pH in a low region and end it in a high region. The concentration of the ligand was increased in relation to the various hydrochloric acid concentrations to accumulate data for three titrations. For metal-ligand titrations, formation constants were determined from four titrations with different ligand-to-metal ratios, namely 1:1, 1:2, 1:3, and 1:4.

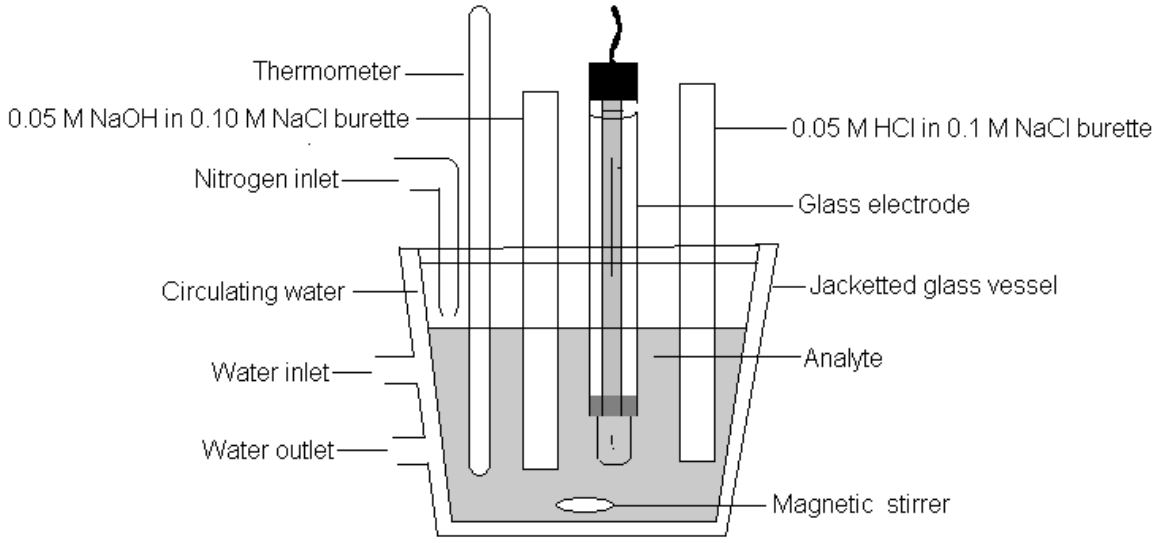

Figure 3.2: *The experimental set-up in the titration vessel.*

3.3 GLASS ELECTRODE POTENTIOMETRY

3.3.1 Glass electrode calibration

The electrode was calibrated after every seven days. The electrode was calibrated with three standard buffer solutions (pH 4.005, pH 7.00 and pH 10.012). The electrode probe was cleaned first before calibration by rinsing it with de-ionised water and gently drying with an absorbent material in order to avoid formation of static charge on the glass. The electrode was then immersed into the first standard buffer solution (pH 4.005), stirred with a magnetic stirrer and allowed to reach equilibrium. The probe was then immersed into the second standard solution (pH 7.00) followed by the third standard solution of pH 10.012 until the electrode stabilized. After each measurement, the probe was rinsed with de-ionised water. The glass probe tip was kept wet at all times when it was not in use to avoid the pH sensing membrane from dehydration which can lead to the electrode being dysfunctional. A 3 M KCl solution was used for this purpose to prevent the diffusion of the electrolyte (KCl) from the liquid junction.

3.3.2 Experimental Procedure

i. Standardization of 0.05 M NaOH in 0.1 M NaCl with potassium hydrogen phthalate (KHP).

An accurate amount of KHP (0.1021 g) was weighed to ensure a concentration of 0.05 M in the 10 ml volume. The KHP was added directly to the vessel for titration. After adding the KHP

crystals to the vessel, 20 ml of 0.15 M NaCl was added and the solution was stirred to dissolve the KHP. The solution was then titrated with 0.05 M NaOH in 0.1 M NaCl at 25°C until the end point was reached. The end point volume was then used to calculate the actual concentration of NaOH.

ii. Determination of E_0 and Gradient (Standard electrode potential)

This was determined daily before titrations. A 5.0 ml solution of 0.05 M HCl in 0.1 M NaCl and a 25 ml solution of 0.15 M NaCl were added into the reaction vessel and then titrated with 0.05 M NaOH in 0.1 M NaCl at 25 °C. The data was refined using the computer program ESTA and the results used for determining the protonation constants of the ligand.

iii. Determination of ligand protonation constants

The protonation constants of the ligand were determined from the following titrations (Table 3.1):

Table 3.1: Composition of protonation titrations for all ligands studied

Titration number	Ligand (0.05 M) (ml)	HCl (0.01 M) (ml)	NaCl (0.15 M) (ml)
1	5	10	25
2	10	10	20
3	15	10	15

iv. Determination of metal- ligand equilibrium constants

After determining protonation constants, metal-ligand complexation titrations were done (Table 3.2):

Table 3.2: Composition of metal-ligand titrations

L:M	0.01 M Ligand in 0.15 M NaCl (ml)	0.05 M HCl in 0.01 M NaCl (ml)	0.15 M NaCl (ml)	$ZrCl_4$ (mg)
1:1	4	10	26	0.009321
1:2	8	10	22	0.009321
1:3	12	10	18	0.009321
1:4	16	10	14	0.009321

Titration data was then analysed with the ESTA library programs for data refinement, and calculation of protonation and complexation formation constants. The pK_w values and hydrolysis constants of Zr(IV) were obtained from the literature and held constant during optimization procedures. Protonation *pKa* values obtained in the titrations without metal ions were fixed during optimization of metal ion titrations. After obtaining a good model, ESTA2A was used to refine E_0 resulting in small changes with improved standard deviations for β values and the Hamilton R-factor.

After successfully determining the formation constants, which was shown by low Hamilton R factors of log β values, the constants were fed into the ECCLES computer program for the simulation of blood plasma and to calculate the plasma mobilization indices.

CHAPTER 4: RESULTS AND DISCUSSIONS

The study of the establishment of a zirconium blood plasma model necessitates the evaluation of the metal ion and its novel chelator with competing blood plasma ligands. Because the overwhelming majority of bioconjugates of Zr^{4+} have utilized DFO as the chelator, this chelator will be included in the discussion [1].

4.1 Zr^{4+} SOLUTION CHEMISTRY

The chemistry of zirconium in water can be best understood in terms of the complexation of Zr^{4+} with OH^- [2]. Zr^{4+} has a high charge density thus it is more likely for the metal ion to undergo hydrolysis in aqueous solutions to give hydroxo complexes. The high charge density makes the ion acidic because the positive metal ion is able to attract electrons in the H-O bonds away from the hydrogens [3]. As a result, the hydrogen atom in the coordinated water molecules will have a positive charge which attracts the water molecules in solution. For example, in the pH range of 0 to 2, the first hydrolysis step of Zr^{4+} is given by the equation

$$Zr^{4+}(nH_2O) = Zr(OH)[(n-1)H_2O]^{3+} + H^+ \quad (4.1)$$

With the final hydrolysis step

$$Zr(OH)_3^+ + H_2O = Zr(OH)_4 + H^+ \quad (4.2)$$

Equation (4.1) and Equation (4.2) show that the complex ion acts as an acid by donating the H^+ to the water molecules in solution [4]. The water molecules in solution also act as a base by accepting H^+. In basic media (1 to 9 M NaOH), the hydrolysis reaction is represented by Equation (4.3)

$$Zr^{4+} + 5H_2O = Zr(OH)_5^- + 5H^+ \quad (4.3)$$

This equation shows that further removal of the H^+ to the water molecules in solution results in an anionic complex [1].

Studies conducted on the hydrolysis of Zr^{4+} ion in aqueous media have also shown evidence of trimetric $[Zr_3(OH)_5]^{7+}$ and tetrametric $[Zr_4(OH)_8]^{8+}$ zirconium complexes in higher-concentration aqueous solutions [4]. The majority of the experimental evidence suggests that the tetrametric species $[Zr_4(OH)_8]^{8+}$ is the predominate oligomeric hydrolysis species in acidic aqueous solutions at higher concentrations [4]. The Zr^{4+} ion is expected to be eight-coodinate in aqueous solution with preference for the square antiprism geometry around the Zr^{4+} ion [5]. The structure of a related oligomeric species which demonstrates the ion-binding ability of the oligers of Zr^{4+} and H_2O and the eight sites capable of ion binding is shown in Figure 4.1.

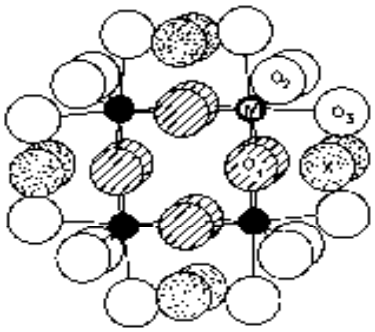

***Figure 4.1**: Structure of the oligomer $Zr_4(OH)_8(H_2O)_{16}X_z^{(8-z)+}(aq)$ as deduced by Muha and Vaughn and reproduced from Baes and Mesmer [1].*

4.1.1 Complexation

Complexation of metal ions in aqueous solution is a process involving the replacement of coordinated water molecules in the solvated cation [6]. The coordinated water molecules act as a ligand that binds, and therefore every complexation reaction in water is effectively a *ligand-exchange* reaction. Metal-ligand complexes can be considered as Lewis acid-base adducts (compounds). Ligands act as Lewis bases (electron pair donors), and the central atom acts as a Lewis acid (electron pair acceptor). Other ligands that can replace water molecules around the central atom (metal ion) are species that have a non bonding pair of electrons to share with the metal [7]. These include simple anions such as the halides (Cl^-, F^-, Br^-, I^-), more complex inorganic compounds such as NH_3, NO_3^-, SO_4^{2-}, CO_3^{2-}, PO_4^{3-}, and a great variety of organic molecules with suitable functional groups, usually containing oxygen, nitrogen, or sulphur atoms as purveyors of electrons pairs (e.g., R–COO^- , R–OH, R– NH_3, R–SH) [8]. However, in this investigation particular emphasis will be on organic molecules with R–COO^- functional group

(e.g. amino acids and fatty acids). The $R–COO^-$ functional group is involved in peptide bonds, and peptides are basically biologically occurring short chains of amino acid monomers. This is important because amino acids are used in the synthesis of proteins which are the most abundant organic molecules in the body [9]. It is therefore these molecules (i.e. molecules with $R–COO^-$ functional groups), that are most likely to disturb the Zr-DFO complex in vivo.

4.1.2 JESS computer program

The physiological ligands with affinity for the Zr^{4+} ion were determined by JESS database and the results are presented in the Table 4.1.

Table 4.1: Reactions of Zr^{4+} with the most probable physiological ligands likely to disturb the Zr-DFO complex *in vivo* and their stability factors as determined by JESS database

Physiological Ligands	Reaction	Temperature (*°C*)	Ionic Charge	Log K
Salicylate	Salicylaldoxime-2 + Zr^{4+} ⇌ Zr^{4+} _Salicylaldoxime-2	25	0 Inf. Dilution	17.9
Aspartate	Asp-2 + Zr^{4+} ⇌ = Zr^{4+} _Asp-2	25	0.1 $NaClO_4$	9.70
Asparaginate	Asn-1 + Zr^{4+} ⇌ Zr^{4+} _Asn-1	25	0.1 $NaClO_4$	8.80
Glutaminate	Gln-1 + Zr^{4+} ⇌ Zr^{4+} _Gln-1	25	0.1 $NaClO_4$	8.75
Citrate	Zr^{4+} + H^{1+}_Citric-3 ⇌ Zr^{4+} _H^{1+}_Citric-3	20	0.1 Unknown	10.80

The JESS database showed that the Zr^{4+} ion is susceptible to forming complexes with many other anions along with molecules of interest in solution. The metal ion showed the capability to form strong complexes with inorganic compounds such as SO_4^{2-} and PO_4^{3-}. However, due to the

focus of this investigation, only organic molecules with the R–COO^- functional group were selected and there were more than ten of these molecules that showed an affinity for the Zr^{4+} ion. The number of these molecules was narrowed down by selecting those that are capable of forming stable complexes with the Zr^{4+} ion (i.e. molecules capable of creating an ML complex with the metal ion). The equations describing the formation of the ML complexes are given in Table 4.1, with the exception of citric acid. Citrate was added to the physiological ligands of interest even though it does not form an ML complex with the metal ion to broaden the study and to get a better understanding.

4.2 AMINO ACIDS

The typical amino acids used in the synthesis of proteins have an α-carbon atom that is attached to an amino (–NH_2) group, a carboxyl (–COOH) group, a hydrogen atom, and a side chain (–R). These are referred to as standard amino acids and they include aspartate, asparaginate and glutaminate (Figure 1.6 and Table 4.1). The standard amino acids differ from each other in the structure of the side chains (–R) bonded to their α-carbon atoms [10]. At pH 7, standard amino acids have their amino group protonated (i.e., the addition of a proton) to form H_3N^+ and their carboxyl group is deprotonated to form –COO^- so that the amino acid exists as;

$$H_3N^+–CHR–COO^- \quad (4.4)$$

This behaviour allows amino acids to be considered as zwitterions, molecules that contain both a positive and a negative charge. At the limits of the pH range, an amino acid will not be a zwitterion. The following acid-base equilibrium tendencies are instances of the reactivity of *free* amino acids.

At very low pH the carboxyl group will become protonated:

$$H_3N^+–CHR–COOH \quad (4.5)$$

At very high pH the amine group loses a proton and becomes uncharged:

$$H_2N–CHR–COO^- \quad (4.6)$$

Even though salicylate and citrate are not amongst the standard amino acids, their presence in the blood plasma is also significant because they also possess the R–COO^- functional group.

Furthermore, the selection of the physiological ligands of interest was also guided by the Linear Free Energy Relationship (LFER). The use of linear free energy relationships (LFER) to determine stability constants relevant to a particular system is a well established approach that can be helpful in elucidating reaction mechanisms and predicting unknown formation constants.

4.3 GLUTAMINATE

4.3.1 Introduction

Glutaminate is an anionic form of the most abundant amino acid in blood, glutamine (Figure 4.3.1). The molecular formula of glutamine is $C_5H_{10}N_2O_3$ with a molecular weight of 146.15 g/mol. It constitutes 60 % of the total free amino acid pool in skeletal muscle and has a concentration of about 2.5 mM in human blood [11].

***Figure 4.3.1**: Structure of glutamine*

Glutamine contains two ionizable (carboxylic and amino) protons in the main chain. The side chain contains a non-basic nitrogen, therefore this amino acid is considered as a neutral type. The neutral amino acids have neither acidic nor basic side chains. These amino acids have their isoelectric points slightly acidic (between 5 and 6) because the H_3N^+– group is slightly more acidic than the $–COO^-$ group is basic [12]. The isoelectric point is the middle pH where the amino acid is balanced between the two states, as a dipolar zwitterion with a net charge of zero.

4.3.2 Results and discussions

The results of modelling using the computer program ESTA are given in Table 4.2. The low Hamilton R factors indicate that the models generated were good fits. These constants closely resemble the values reported in the literature [13].

Table 4.2: Protonation constants of glutamine and equilibrium constants of Zr(IV) complexation with glutamine as determined by glass electrode potentiometry and ESTA modelling at 25 °C and ionic strength of 0.15 mol.dm^{-3} NaCl.

Equilibrium Species [#]	**Log β (*25 ºC*)**		**Hamilton R-factor**	**Number of points**
	This work	Literature[13]		
	0.15 M NaCl	*0.1 M NaCl*		
Glutamine				
$H + L \rightleftharpoons HL$	8.99 ± 0.01	9.00 ± 0.03	0.02710	146
$2H + L \rightleftharpoons H_2L$	2.39 ± 0.02	2.18 ± 0.03		
$Zr(IV) - H \rightleftharpoons Zr(IV)H_{-1}$	0.51			
$Zr(IV) - 5H \rightleftharpoons Zr(IV)H_{-5}$	-14.95			
$3Zr(IV) - 4H \rightleftharpoons Zr(IV)H_{-4}$	0.24			
$4Zr(IV) - 8H \rightleftharpoons Zr(IV)H_{-8}$	-4.32			
$M + L – H \rightleftharpoons MLH_{-1}$	23.11		0.05798	216
$M + L - 2H \rightleftharpoons MLH_{-2}$	19.04 ± 0.02			
$M + L - 3H \rightleftharpoons MLH_{-3}$	9.75 ± 0.03			
$M + L - 4H \rightleftharpoons MLH_{-4}$	-1.08 ± 0.07			

[#]*The charges on Zr(IV) ions, glutaminate, protons and complexes are omitted for simplicity.*

** Hydrolysis constants for Zr(IV) are obtained from literature [14] and included in the model. They are expressed as ZrH_{-x} instead of the normal $Zr(OH)_x$ because the ESTA program uses this format as input.*

4.3.3 Glutamine protonation (ionization)

The protonation curve for glutaminate is shown in Figure 4.3.2. The calculated data, $\overline{Z}_H$ (represented by the solid line) follows the experimental data (points) very closely. From the $\overline{Z}_H$ curves, it can be seen that the ligand loses two protons, one in the acidic region at pH 2.2 and the second one in the basic region at pH 9.

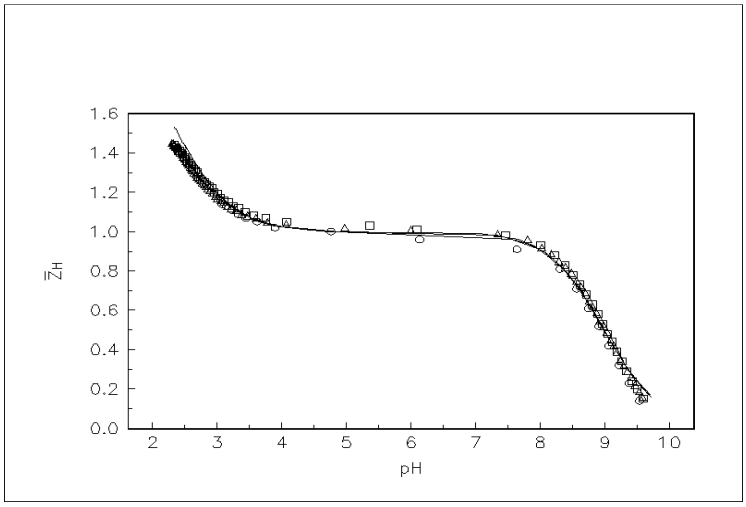

***Figure 4.3.2**: $\overline{Z}_H$ curves for the protonation of glutamine. Experimental (symbols) and theoretical (lines) protonation formation curves for glutamine. The experimental points represent each titration by (O) 0.00165287 M glutamine, 0.00821904 M HCl, (□) 0.0033126 M glutamine, 0.0080423 M HCl and (Δ) 0.0049792 M glutamine, 0.0083447 M HCl.*

$\overline{Z}_H$ and the number of moles of alkali consumed per mole of ligand are useful in detecting the number of equilibria. For example, the protonation constants of the ligand can be deduced from pH values at half integral values of $\overline{Z}_H$ based on their correspondence. The overlapping plots (Figure 4.3.2) at various concentrations rule out the possibility of polymerization of the ligand molecules [11]. However, the $\overline{Z}_H$ versus pH plots (Figure 4.3.2) do not show the percentage of the species present in the pH range being studied. Therefore it is important to form a speciation curve of $\overline{Z}_H$ versus pH to better evaluate the present species in the pH range of interest. The pH of the blood is around 7.4 therefore the species distribution can give a clear indication of the existence of the ligand at that specific pH.

The speciation distribution curves presented in Figure 4.3.3 shows that the ligand exists mostly as LH at pH 7.4 constituting 95 % mole fraction of the total ligand concentration with existence

of L constituting 5 % mole fraction. LH_2 on the other hand appears to only exist at the pH < 6 as expected since it decreases with the deprotonation of the carboxyl group. Therefore this ligand forms LH_2 at low pH and gets deprotonated with the formation of LH and L successively as the pH increases.

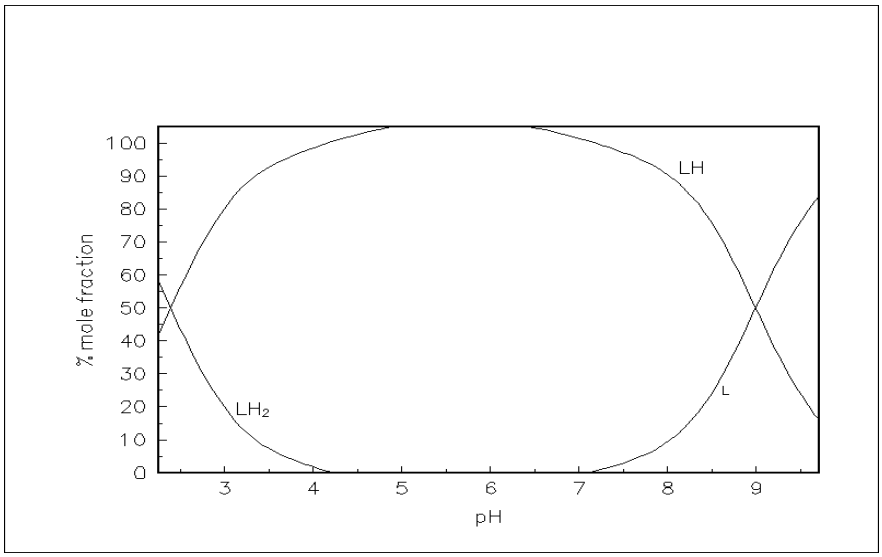

Figure 4.3.3*: Speciation distribution curve for the protonation of glutamine plotted as a function of pH at 25 °C and 0.15 M NaCl. Concentrations used were 0.00165287 M glutamine and 0.00821904 M HCl.*

4.3.4 Complexation of Zr(IV) with glutaminate

Good models were obtained using 1:1, 3:1 and 4:1 ligand to metal concentration ratios (Table 4.2). The curves from the experimental data and the theoretical ones were refined to produce the $\overline{Q}$ and $\overline{Z}$ curves so that the results could be interpreted. The $\overline{Q}$ curve is the deprotonation function, representing the average number of protons released on complexation per metal-ion and the dashed curve that appears along with it in the model is the $\overline{n}$ curve, which represents the deprotonation of the free ligand. $\overline{Z}$ represents the complexation function, the number of ligands bound per metal. Figure 4.3.4 shows the $\overline{Z}$ curve obtained from Zr(IV)-glutaminate complexation in this study.

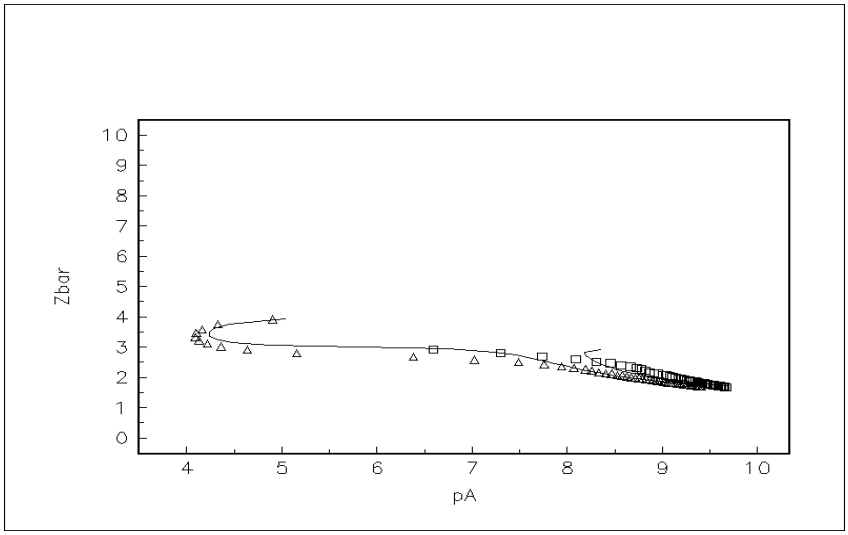

***Figure 4.3.4**: $\overline{Z}$ curves for the complexation of glutamine with Zr(IV). Experimental (3:1 (□) and 4:1 (Δ)) and theoretical (lines) formation for Zr(IV) complexation by glutaminate. The experimental points represent each titration by (□) 0.0030038 M glutamine, 0.0010139 M Zr(IV), 0.0126190 M HCl and (Δ) 0.0039862 M glutamine, 0.0010041 M Zr(IV), 0.0123913 M HCl. pA is the negative log of the free ligand concentration.*

The complexes formed by Zr(IV)-glutaminate appear to be all hydroxyl species as seen from Figure 4.3.5. The $\overline{Q}$ curves are always above the $\overline{n}$ curve, indicating that the number of protons lost is higher than the amount of protons on the ligand without metal ion. The presence of the hydroxyl species is further supported by the backfanning on the $\overline{Z}$ curves and the high charge of Zr(IV) which suggests that the metal ion is surrounded by water molecules. These water molecules can also lose protons as the pH increases.

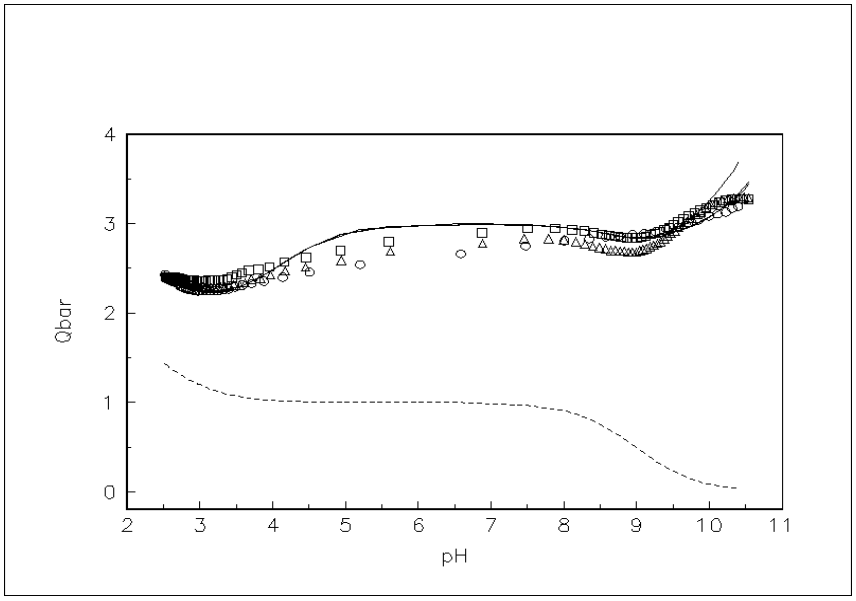

***Figure 4.3.5**: $\overline{Q}$ curves for the complexation of glutamine with Zr(IV). Experimental (1:1 (O), 3:1 (□) and 4:1 (Δ)) and theoretical (lines) deprotonation formation curves for Zr(IV) complexation by glutaminate. The experimental points represent each titration by (O) 0.0010030 M glutamine, 0.001001 M Zr(IV), 0.0123848 M HCl, (□) 0.0030038 M glutamine, 0.0010139 M Zr(IV), 0.0126190 M HCl and (Δ) 0.0039862 M glutamine, 0.0010041 M Zr(IV), 0.0123913 M HCl.*

The representation of the species distribution of complexation of Zr(IV)-glutaminate is shown in Figure 4.3.6. There are five species present across the pH of the study, MLH_{-1}, MLH_{-2}, MLH_{-3}, MH_{-4} and MH_{-5}. The MLH_{-2} species is predominant over a wide pH range (from 4 to 9) giving 100 % mole fraction concentration of the complex at pH 6.5. It is the predominant species at the physiological conditions (pH 7.4) with a percentage mole fraction of 98 %, with only a 2 % mole fraction belonging to MLH_{-3}.

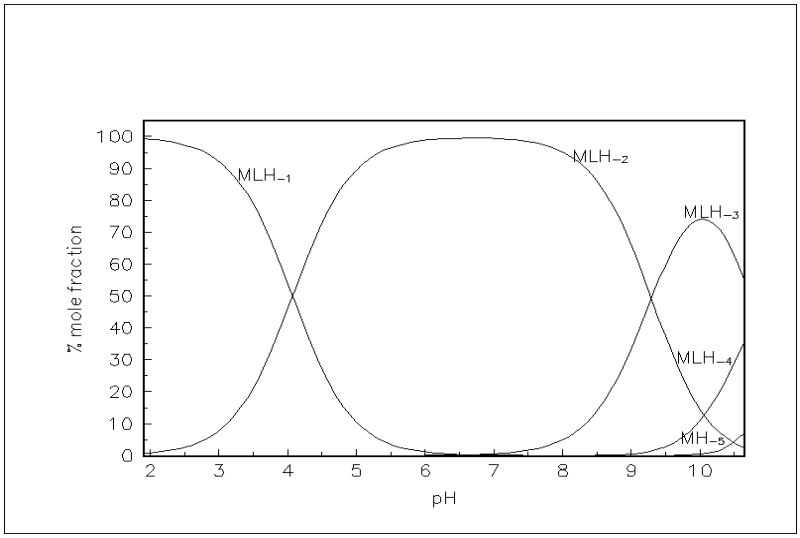

***Figure 4.3.6**: Speciation distribution curve of Zr(IV) complexation by glutaminate plotted as a function of pH at 25 °C and 0.15 M ionic strength. Concentrations used were 0.0010041 M Zr(IV), 0.0039862 M glutamine and 0.0123913 M HCl.*

When looking at the $\overline{Q}$ curve and the speciation curve, there is a deviation of the data points from the theoretical curve in the $\overline{Q}$ curves that occurs with the formation MLH_{-2} in the speciation curves. This deviation is the result of the Zr(IV) metal ions hydrolysing to form the MLH_{-2} complex. The maximum deviation is seen at pH 5.5 where the species reaches its maximum percentage mole fraction. There is also some deviation appearing towards the end of the pH range in the $\overline{Q}$ curves due to the formation of the MH_{-5} complex. At this stage during the titrations the ligand had lost all the available protons, therefore the metal ion could only form complexes with the hydroxy species which then precipitate.

4.4 ASPARTATE

4.4.1 Introduction

Aspartates are salts and carboxylate anions of aspartic acid. Aspartic acid is a polar amino acid with the chemical formula $HOOCCH(NH_2)CH_2COOH$ [15]. The negative charge of aspartates means that they can interact with positively charged non-protein atoms, such as cations like zirconium. Aspartates are involved in removal of ammonia and other toxins from the blood [16]. The structure of aspartic acid is given in Figure 4.4.1.

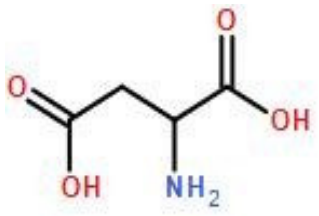

***Figure 4.4.1**: Structure of aspartic acid*

The structure (Figure 4.4.1) shows that aspartic acid also contains two ionizable (carboxylic and amino) protons on the main chain. However, unlike glutamine, aspartic acid contains a side chain that is not neutral. The side chain contains another ionizable proton on the carboxylic acid, therefore this amino acid is considered as the acidic type. The two ionizable carboxylic protons are deprotonated and have negative charges at pH 7 [12]. When the side chain is deprotonated, aspartic acid is more appropriately called aspartate.

4.4.2 Results and discussions

The results of modelling using the computer program ESTA are given in Table 4.3. The low Hamilton R factors indicate that the models generated were good fits. The constants obtained also resemble the values reported in literature [13].

Table 4.3: Protonation constants of aspartic acid and equilibrium constants of Zr(IV) complexation with aspartic acid as determined by glass electrode potentiometry and ESTA modelling at 25 °C and ionic strength of 0.15 mol.dm^{-3} NaCl.

***Equilibrium Species*[#]**	**Log β (*25 ºC*)**		**Hamilton R-factor**	**Number of points**
	This work	Literature[13]		
	0.15 M NaCl	*0.1 M NaCl*		
Aspartic acid				
$H + L \rightleftharpoons HL$	9.63 ± 0.02	9.65 ± 0.08	0.03888	338
$2H + L \rightleftharpoons H_2L$	4.05 ± 0.02	3.70 ± 0.05		
$3H + L \rightleftharpoons H_3L$	1.93 ± 0.08	1.90 ± 0.1		
$Zr(IV) - H \rightleftharpoons Zr(IV)H_{-1}$	0.51			
$Zr(IV) - 5H \rightleftharpoons Zr(IV)H_{-5}$	-14.95			
$3Zr(IV) - 4H \rightleftharpoons Zr(IV)H_{-4}$	0.24			
$4Zr(IV) - 8H \rightleftharpoons Zr(IV)H_{-8}$	-4.32			
$M + L \rightleftharpoons ML$	29.26 ± 0.03		0.05126	204
$M + L - H \rightleftharpoons MLH_{-1}$	26.28			
$M + L - 2H \rightleftharpoons MLH_{-2}$	19.44 ± 0.04			
$M + L - 3H \rightleftharpoons MLH_{-3}$	9.43 ± 0.05			

[#] *The charges on Zr(IV) ions, aspartate, protons and complexes are omitted for simplicity.*

** Hydrolysis constants for Zr(IV) are obtained from literature [14] and included in the model. They are expressed as ZrH_{-x} instead of the normal $Zr(OH)_x$ because the ESTA program uses this format as input.*

4.4.3 Aspartic acid protonation (ionization)

The protonation curve for the aspartic acid is shown in Figure 4.4.2. The calculated data, $\overline{Z}_H$ (represented by the solid line) follows the experimental data (points) very closely.

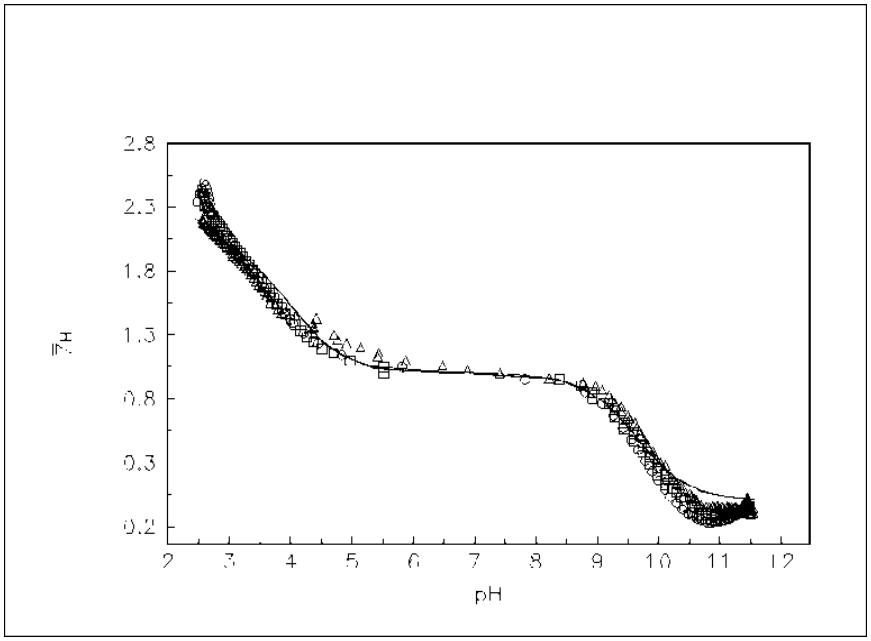

***Figure 4.4.2**: $\overline{Z}_H$ curves for the protonation of aspartic acid. Experimental (symbols) and theoretical (lines) protonation formation curves for aspartic acid. The experimental points represent each titration by (O) 0 .0016528 M aspartic acid, 0.0082988 M HCl, (□) 0.0033126 M aspartic acid, 0.0082590 M HCl and (Δ) 0.0049792 M aspartic acid, 0.0082761 M HCl.*

The representation of the species distribution of protonation of aspartic acid across the pH of this study is shown in Figure 4.4.3. The ligand proved to have three ionizable protons; the first two are the carboxylic acid protons (LH_3 and LH_2), and the last is the ammonium proton (LH). At the physiological condition (pH 7.4), both protons from the carboxyl groups, LH_3 and LH_2, are deprotonated as expected and the only existing species is the LH with 100 % mole fraction. In this system the ligand starts to lose its final proton (LH) at pH 8 and the free ligand (L) becomes predominant at pH 9.7.

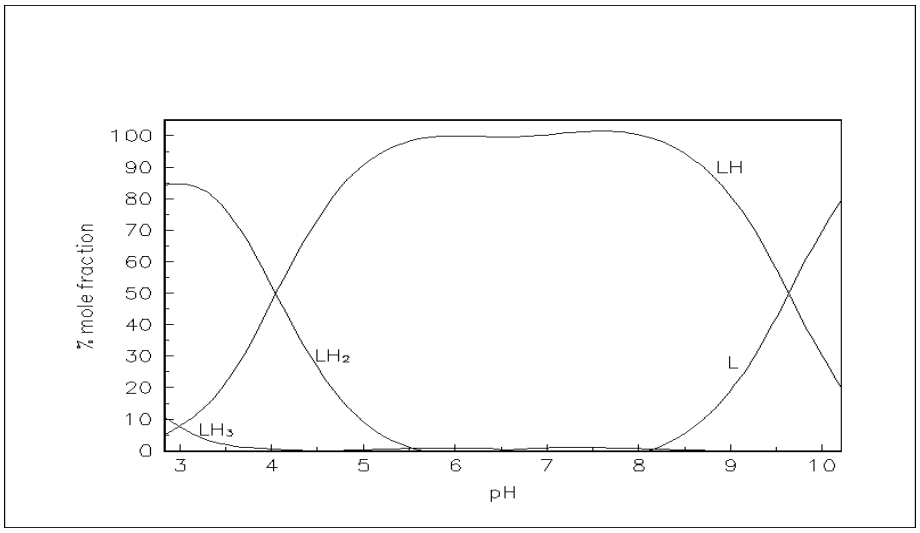

***Figure 4.4.3**: Speciation distribution curve for the protonation of aspartic acid plotted as a function of pH at 25 °C and 0.15 M NaCl. Concentrations used were 0.0033126 M aspartic acid and 0.0082590 M HCl.*

4.4.4 Complexation of Zr(IV) with aspartate

In the complexiometric titrations of Zr(IV)-aspartate good models were obtained from using higher ligand to metal concentration ratios (2:1, 3:1, and 4:1).The modelled curves of the $\overline{Z}$ curves (Figure 4.4.4) also showed some evidence of hydrolysis indicated by back fanning.

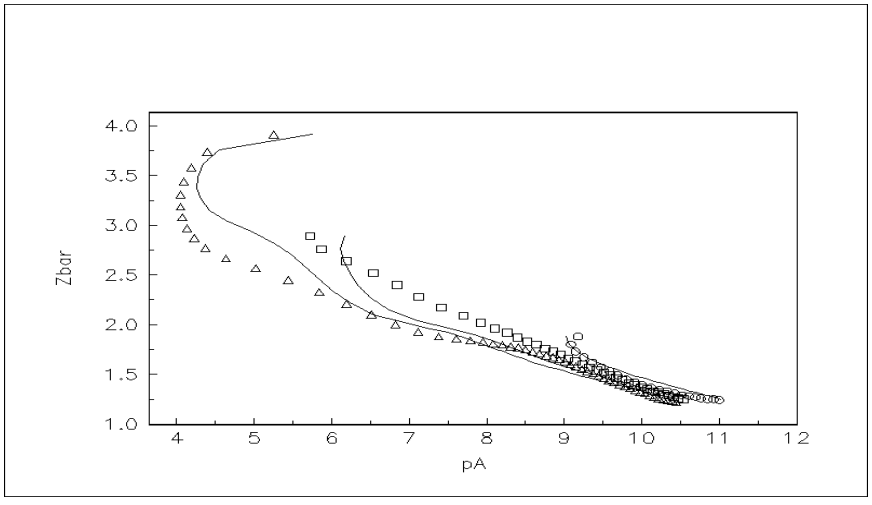

***Figure 4.4.4**: $\overline{Z}$ curves for the complexation of aspartate with Zr(IV). Experimental (O, □ and ∆) and theoretical (lines) formation for Zr(IV) complexation by aspartate. The three separate titrations are represented by (O) 0.0019892 M aspartic acid, 0.0010129 M Zr(IV) 0.0125817 M*

HCl (□) 0.0029868 M aspartic acid 0.0010031 M Zr(IV), 0.0125816 M HCl and (Δ) 0.0039462 M aspartic acid, 0.0010041 M Zr(IV), 0.0124521 M HCl.

$\overline{Q}$ curves (Figure 4.4.5) are above the $\overline{n}$ throughout the titrations also indicating that the number of protons lost is higher than the number of protons on the ligand without a metal ion. This supports the evidence of formation of hydrolysis species shown by the backfanning of $\overline{Z}$ curves. The interpretation of both $\overline{Q}$ and $\overline{n}$ helps in determining the complexes that forms, ML, $MLH_{-1,}$ MLH_{-2}, MLH_{-3} and MLH_{-5}. These complexes can be seen clearly in the representation of the species distribution of Zr(IV)-aspartate shown in Figure 4.4.6.

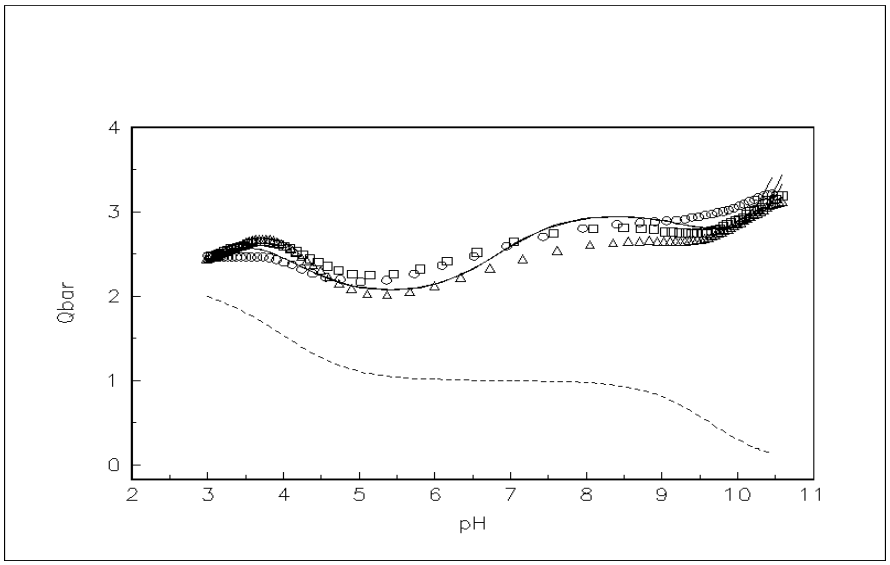

***Figure 4.4.5**: $\overline{Q}$ curves for the complexation of aspartate with Zr(IV). Experimental (2:1 (O), 3:1 (□) and 4:1 (Δ)) and theoretical (lines) deprotonation formation curves for Zr(IV) complexation by aspartate. The three separate titrations are represented by (O) 0.0019892 M aspartic acid, 0.0010129 M Zr(IV) 0.0125817 M HCl (□) 0.0029868 M aspartic acid, 0.0010031 M Zr(IV), 0.0125816 M HCl and (Δ) 0.0039462 M aspartic acid, 0.0010041 M Zr(IV), 0.0124521 M HCl.*

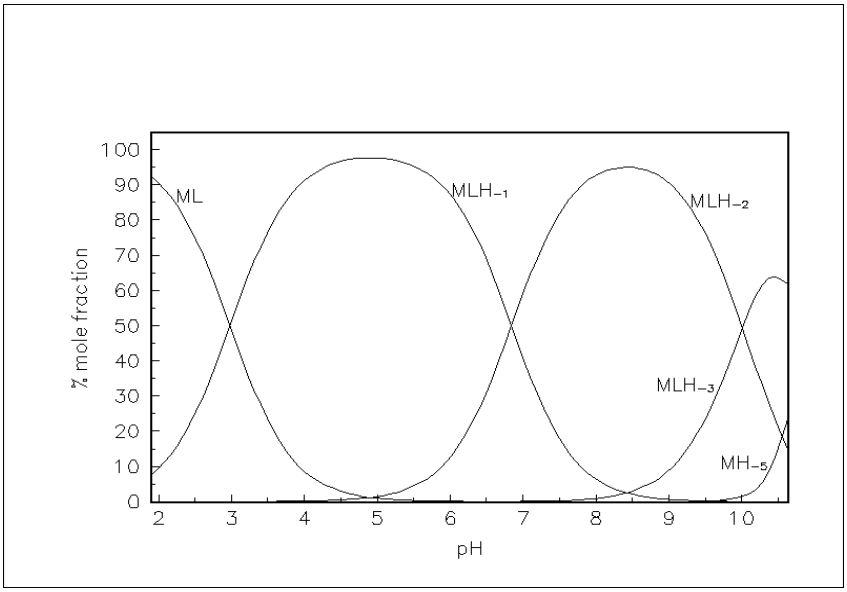

Figure 4.4.6*: Speciation distribution curve of Zr(IV) complexation by aspartate plotted as a function of pH at 25 °C and 0.15 M ionic strength. Concentrations used were 0.0029868 M aspartic acid, 0.0010031 M Zr(IV), and 0.0125816 M HCl.*

The speciation distribution curve of Zr(IV)-aspartate (figure 4.4.6) shows that there are five complexes, with ML predominating at pH < 3 reaching a maximum of more than 90% followed by MLH_{-1} predominating in the pH range 3-7 reaching a maximum of 95 % mole fraction of the total complex concentration. At physiological conditions (pH 7.4) the species present are MLH_{-1} with 25 % and MLH_{-2} with 75 % mole fraction of the total complex concentration. MLH_{-3} predominates at pH 10.5 (60 % mole fraction) and MH_{-5} exist at pH > 9.8. The formation of MLH_{-2} at pH 4.5 explains the deviations in $\overline{Q}$ data through hydrolysis of Zr(IV) ions to form the complex. These deviations extends throughout the region where the complex exists, reaching their maximum where the mole fraction of the complex reaches its maximum at pH 8. Similar behaviour was also observed in the previously discussed Zr(IV)-glutaminate complexation with the $\overline{Q}$ data showing some deviations in the region where the MLH_{-2} species started forming reaching maximum deviation from the theoretical curve in the region where the mole fraction of the species reached its maximum. Also in this part of the investigation, the deviation that occurs at the end of the pH range can be associated with the formation of MH_{-5}.

4.5 ASPARAGINATE

4.5.1 Introduction

Asparaginate is a standard amino acid anion that is the conjugate base of asparagines (Figure 4.5.1). Asparagine can hydrolyse to form aspartic acid; therefore it plays the same role as aspartic acid in the blood plasma. It has one carboxamide group on the side chain with one amino and carboxyl group on the alpha carbon atom. It is a neutral, polar and uncharged amino acid in any biologically relevant pH conditions [17].

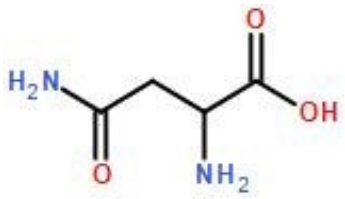

***Figure 4.5.1**: Structure of asparagine*

The structure (Figure 4.5.1) shows that asparagine contains two ionizable (carboxylic and amino) protons on the main chain. The side chain contains a non-basic nitrogen atom, therefore this amino acid is considered as a neutral type. The overall molecule of asparagine is therefore uncharged and exists in the form of a zwitter ion like glutamine. In acidic medium, the zwitterion exists in the form of a positively charged ion and move towards the cathode during electrolysis. While in a basic medium, it exists in the form of a negatively charged ion and move towards the anode [17].

4.5.2 Results and discussions

The results of modelling using the computer program ESTA are given in Table 4.4. The low Hamilton R factors indicate that the models generated were good fits. The constants obtained also resemble the values reported in the literature [13].

Table 4.4: Protonation constants of asparagine and equilibrium constants of Zr(IV) complexation with asparagine as determined by glass electrode potentiometry and ESTA modelling at 25 °C and ionic strength of 0.15 mol.dm^{-3} NaCl.

Equilibrium Species [#]	**Log β (*25 ºC*)**		**Hamilton R-factor**	**Number of points**
	This work	Literature[13]		
	0.15 M NaCl	*0.1 M NaCl*		
Asparagine				
$H + L \rightleftharpoons HL$	8.87 ± 0.005	8.72 ± 0.02	0.02018	221
$2H + L \rightleftharpoons H_2L$	2.44 ± 0.007	2.15 ± 0.01		
$Zr(IV) - H \rightleftharpoons Zr(IV)H_{-1}$	0.51			
$Zr(IV) - 5H \rightleftharpoons Zr(IV)H_{-5}$	-14.95			
$3Zr(IV) - 4H \rightleftharpoons Zr(IV)H_{-4}$	0.24			
$4Zr(IV) - 8H \rightleftharpoons Zr(IV)H_{-8}$	-4.32			
$M + L \rightleftharpoons ML$	24.24		0 .03878	220
$M + L – H \rightleftharpoons MLH_{-1}$	22.38 ± 0.02			
$M + L - 2H \rightleftharpoons MLH_{-2}$	18.51			
$M + L - 3H \rightleftharpoons MLH_{-3}$	9.93 ± 0.02			
$M + L - 4H \rightleftharpoons MLH_{-4}$	-0.34 ± 0.02			

[#]*The charges on Zr(IV) ions, asparagine, protons and complexes are omitted for simplicity.*

** Hydrolysis constants for Zr(IV) are obtained from literature [14] and included in the model. They are expressed as ZrH_{-x} instead of the normal $Zr(OH)_x$ because the ESTA program uses this format as input.*

4.5.3 Asparagine protonation (ionization)

The protonation curve for asparagine is shown in Figure 4.5.2. The calculated data, $\overline{Z}_H$ (represented by the solid line) follows the experimental data (points) very closely.

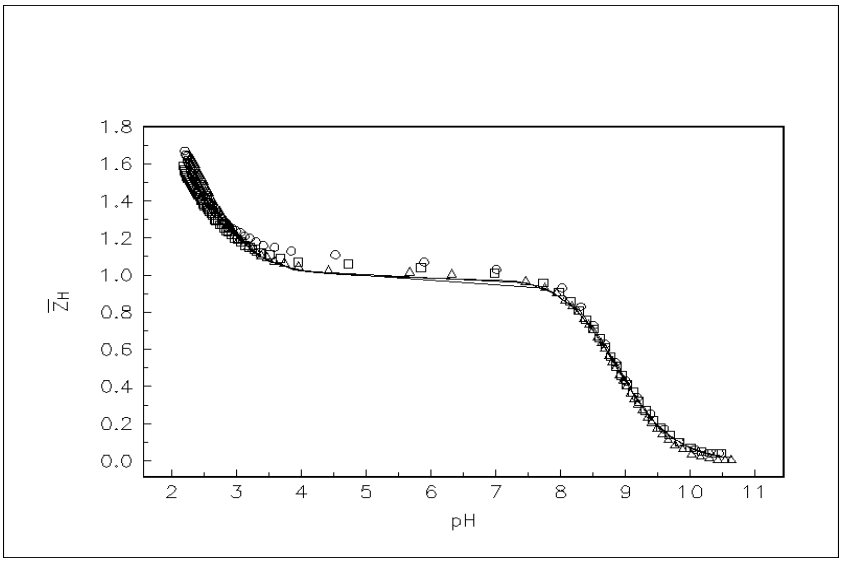

Figure 4.5.2*: $\overline{Z}_{\mathrm{H}}$ curves for the protonation of Asparagine. Experimental (symbols) and theoretical (lines) protonation formation curves for asparagine. The titrations are represented by (O) 0.00166023 M asparagine, 0.00839034 M HCl, (□) 0.00332367 M asparagine, 0.00839646 M HCl and (Δ) 0.00499033 M asparagine, 0.00839789 M HCl.*

The asparagine ligand studied also proved to have two ionizable protons, similar to glutamine. This is also illustrated in the species distribution (Figure 4.5.3) with the ligand having the neutral form (LH) being the predominant species in the pH region extending from 2.5 to 8.9 which includes the physiological condition (pH 7.4). The ligand only exists in the fully protonated form (LH_2) in an acidic solution (pH < 4.5). The ligand therefore only exists as LH at the blood pH (i.e. pH 7.4) with 100 % mole fraction. The concentration of the fully deprotonated ligand (L) only starts raising more than zero at pH 7.5 and becomes the predominant species at pH > 9.

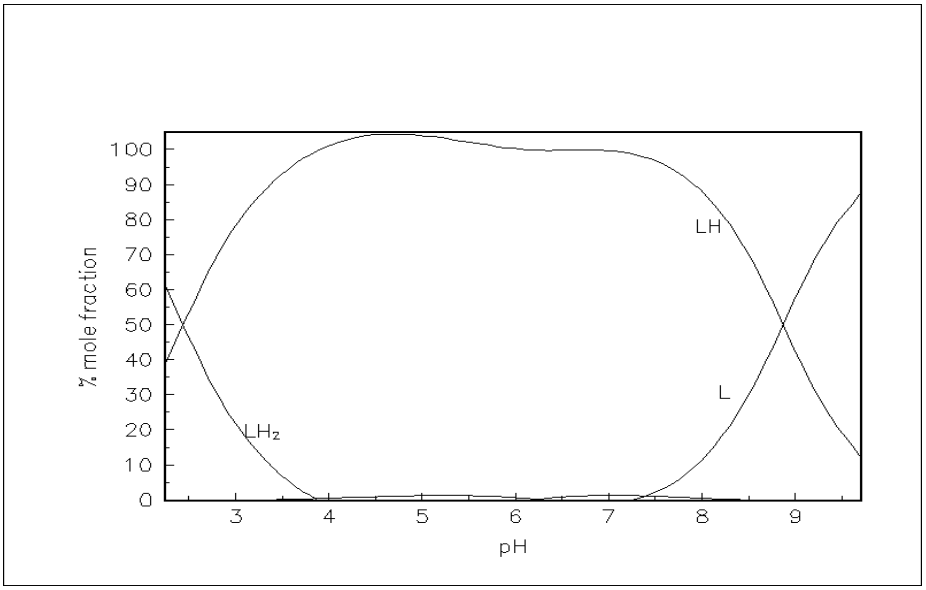

Figure 4.5.3*: Speciation distribution curve for the protonation of asparagine plotted as a function of pH at 25 °C and 0.15 M NaCl. Concentrations used were 0.00166023 M asparagine and 0.00839034 M HCl.*

4.5.4 Complexation of Zr(IV) with asparagine

The good model curves were also obtained from using higher ligand to metal concentration ratios (2:1, 3:1, and 4:1) in the Zr(IV)-asparagine complexiometric titrations. These ratios produced better curves compared to the 1:1 ratio because of the precipitation of Zr(IV) when complexed to amino acids. The metal evidently formed a precipitate because of the positive charge on the ligand $[LH_2]^+$ due to the amino group ($-NH_3^+$) at low pH. At this stage of the titration, the ligand had no electrons to donate so the metal ion formed an insoluble complex with the hydroxy species. The $\overline{Z}$ curves (Figure 4.5.4) also showed some evidence of hydrolysis indicated by back fanning. The $\overline{Z}$ curves are also not overlapping which also indicates the presence of polynuclear species.

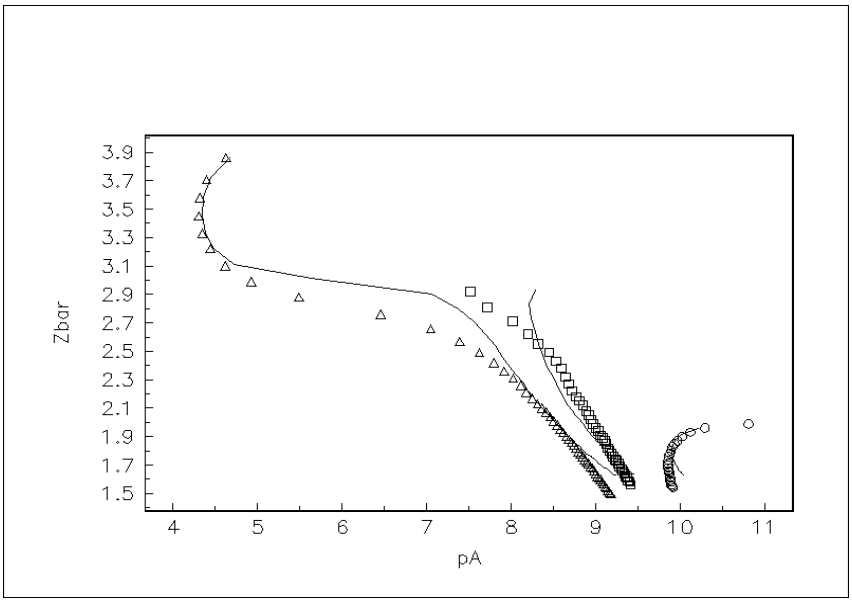

***Figure 4.5.4**: $\overline{Z}$ curves for the complexation of asparagine with Zr(IV). Experimental (2:1 (O), 3:1 (□) and 4:1 (Δ)) and theoretical (lines) formation for Zr(IV) complexation by asparaginate. The three separate titrations are represented by (O) 0.0019892 M asparagine, 0.0009913 M Zr(IV), 0.0125147 M HCl and (□) 0.0029868 M asparagine, 0.0010031 M Zr(IV), 0125270 M HCl and (Δ) 0.0039862 M asparagine, 0.0009932 M Zr(IV), 0.0124793 M HCl.*

The $\overline{Q}$ curves of Zr(IV)-asparaginate (Figure 4.5.5) also indicate the presence of hydroxo and mixed hydroxo complexes . In this system, the $\overline{n}$ is also below the $\overline{Q}$ throughout the titrations, which is interpreted as more protons being detected at the electrode than expected. This implies that there are protons lost from the coordinated water molecules.

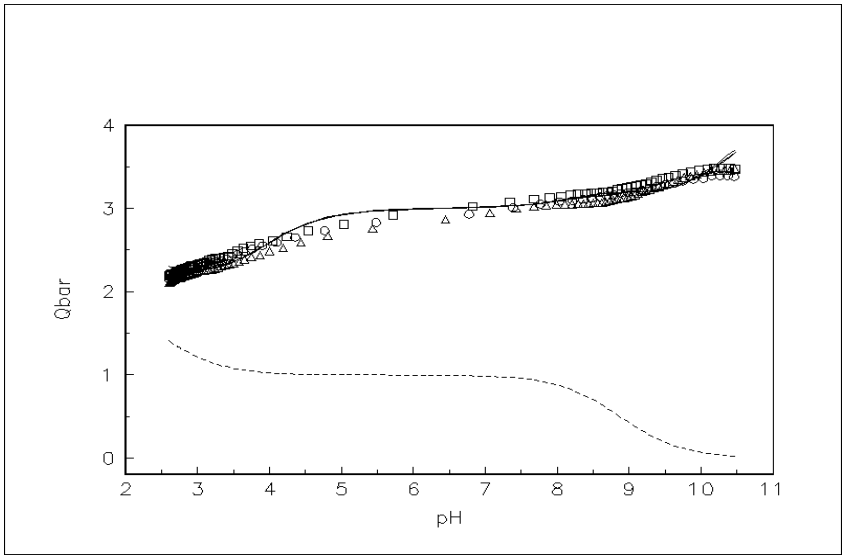

***Figure 4.5.5**: $\overline{Q}$ curves for the complexation of asparagine with Zr(IV). Experimental (2:1 (O), 3:1 (□) and 4:1 (Δ)) and theoretical (lines) deprotonation formation curves for Zr(IV) complexation by asparaginate. The three separate titrations are represented by (O) 0.0019892 M asparagine, 0.0009913 M Zr(IV) 0.0125147 M HCl and (□)0.0029868 M asparagine, 0.0010031 M Zr(IV) 0.0125270 M HCl and (Δ)0.0039862 M asparagine, 0.0009932 M Zr(IV) 0.0124793 M HCl.*

Using the $\overline{Q}$ curves in Figure 4.5.5 the first species that is forming at pH 2.5 can be calculated; At pH 2.5 $\overline{Q}$ is at 2, therefore in the presence of the metal ions, two protons are lost on complexation per metal ion and the complex that forms is

$$M + LH_2 - 2H \rightleftharpoons ML \qquad (4.7)$$

This species should therefore be the first species that appear in the species distribution curves because the $\overline{Q}$ curves show that it is predominant in the highly acidic region. Even though the equilibrium in Equation 4.7 shows that species can be calculated from the $\overline{Q}$ curves, the speciation distribution curves provide an easier and more effective method for interpretation of results.

The speciation curves of Zr(IV)-asparagine is shown in Figure 4.5.6. These curves represent various species present from low to high pH throughout the titrations, namely ML, MLH_{-1}, MLH_{-2}, MLH_{-3}, MLH_{-4} and MH_{-5}. The ML species appears to be predominant in the low pH region thus corroborating calculation of the equilibrium Equation 4.7. At pH 7.4 (physiological conditions),

the predominant species is MLH_{-2} with 90 % followed by MLH_{-3} with only 10 % mole fraction. MLH_{-3} is predominant at pH 9.5 (80 % mole fraction) where the ligand is negatively charged after losing a proton on the amino group. MLH_{-4} starts to form at pH 8.5, reaching above 60 % at pH 10.5 while the MH_{-5} starts to form after the ligand has fully been deprotonated at pH 9.5. The slight deviation at the end of the pH range can also be attributed to the formation of MH_{-5}.

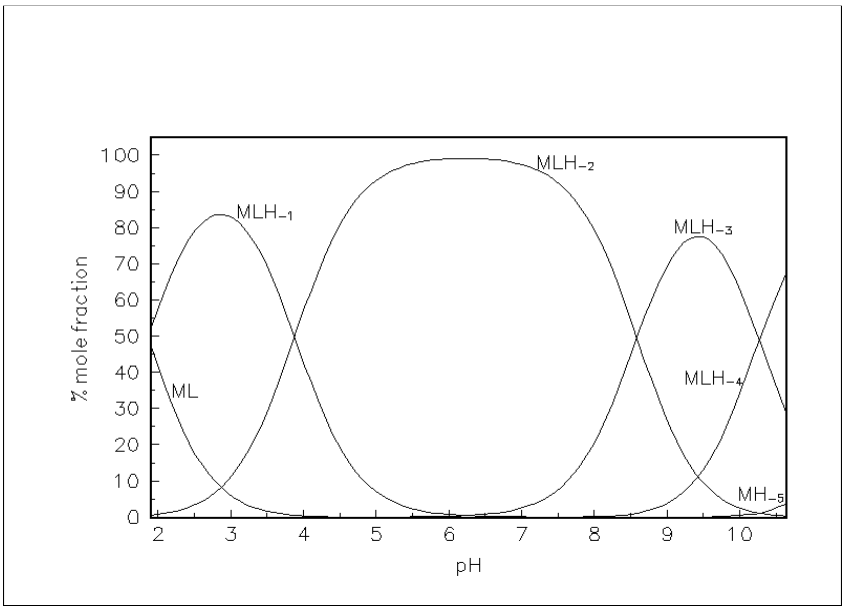

Figure 4.5.6*: Speciation distribution curve of Zr(IV) complexation by asparaginate plotted as a function of pH at 25 °C and 0.15 M ionic strength. Concentrations used were 0.0029868 M asparagine, 0.0010031 M Zr(IV), 0.0125270 M HCl.*

The MLH_{-2} species which also caused deviations in the earlier discussed amino acids also presented the same problem in this part of the experimentation. As it can be seen from the species distribution curves (Figure 4.5.6), the maximum deviation of the theoretical curve and the data points coincides with the maximum percent mole fraction of the MLH_{-2} species (i.e. pH 5) in the $\overline{Q}$ curves (Figure 4.5.5). This species forms when the ligand is neutral, after deprotonation of the carboxyl group which is a possible site for complexation. This is observed in the species distribution curves of the free ligands (Figure 4.3.3, Figure 4.4.3 and Figure 4.5.3) and $\overline{Q}$ curves (Figure 4.3.5, Figure 4.4.5 and Figure 4.5.5) of the metal-ligand complex formation in glutaminate, aspartate and asparaginate. In the curves, as the mole fraction of the LH_2 decreases (i.e. deprotonation at the carboxyl group) the mole fraction of the MLH_{-2} rises.

4.6 SALICYLIC ACID

4.6.1 Introduction

Salicylaldoxime is an oxime of salicylaldehyde described by the formula $C_6H_4CH=NOH$-2-OH. Salicylaldehyde is the main derivative of salicylic acid along with acetylsalicylic acid (aspirin), methylsalicylate and salicyl [18]. Aspirin and other salicylates are rapidly metabolized to salicylic acid which has a plasma half life of roughly six hours after ingestion [19]. Salicylic acid has the formula $C_6H_4(OH)COOH$, where the OH group is ortho to the carboxyl group (i.e. the $R–COO^-$ functional group). It is also known as 2-hydroxybenzoic acid. The structure of salicylic acid is shown in Figure 4.6.1.

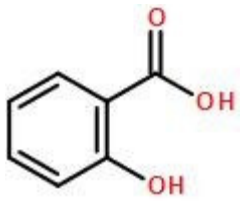

***Figure 4.6.1**: Structure of salicylic acid*

The structure (Figure 4.6.1) shows that salicylic acid contains two ionizable (carboxylic and OH groups) protons.

4.6.2 Results and discussions

The results of modelling using the computer program ESTA are given in Table 4.5. The low Hamilton R factors indicate that the models generated were good fits. The constants obtained also resemble the values reported in the literature [13].

Table 4.5: Protonation constants of salicylic acid and equilibrium constants of Zr(IV) complexation with salicylic acid as determined by glass electrode potentiometry and ESTA modelling at 25 °C and ionic strength of 0.15 mol.dm^{-3} NaCl.

***Equilibrium Species*[#]**	**Log β (*25 ºC*)**		**Hamilton R-factor**	**Number of points**
	This work	Literature[13]		
	0.15 M NaCl	*0.1 M NaCl*		
Salicylic acid				
$H + L \rightleftharpoons HL$	13.20 ± 0.76	13.14 ± 0.2	0.02882	197
$2H + L \rightleftharpoons H_2L$	2.93 ± 0.76	2.80 ± 0.04		
$Zr(IV) - H \rightleftharpoons Zr(IV)H_{-1}$	0.51			
$Zr(IV) - 5H \rightleftharpoons Zr(IV)H_{-5}$	-14.95			
$3Zr(IV) - 4H \rightleftharpoons Zr(IV)H_{-4}$	0.24			
$4Zr(IV) - 8H \rightleftharpoons Zr(IV)H_{-8}$	-4.32			
$M + L - H \rightleftharpoons MLH_{-1}$	31.66 ± 0.05		0.08067	145
$M + L - 2H \rightleftharpoons MLH_{-2}$	24.93			
$M + L - 3H \rightleftharpoons MLH_{-3}$	13.24 ± 0.12			

[#] *The charges on Zr(IV) ions, salicylate, protons and complexes are omitted for simplicity.*

** Hydrolysis constants for Zr(IV) are obtained from literature [14] and included in the model. They are expressed as ZrH_{-x} instead of the normal $Zr(OH)_x$ because the ESTA program uses this format as input.*

4.6.3 Salicylic acid protonation (ionization)

The protonation curve for the salicylic acid is shown in Figure 4.6.2. The calculated data, $\overline{Z}_H$ (represented by the solid line) follows the experimental data (points) very closely.

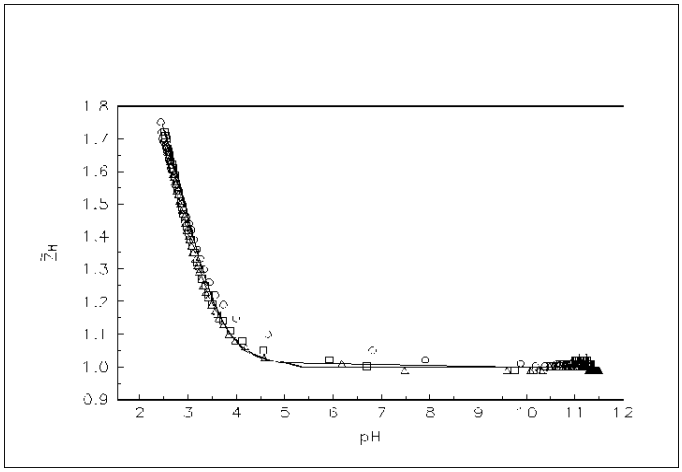

***Figure 4.6.2**: $\overline{Z}_H$ curves for the protonation of salicylic acid. Experimental (symbols) and theoretical (lines) protonation formation curves for salicylic acid. The titrations are represented by (O) 0.001660 M salicylic acid, 0.008389 M HCl, (□) 0.003324 M salicylic acid, 0.008391 M HCl and (Δ) 0.004990 M salicylic acid, 0.008416 M HCl.*

The species distribution curves (Figure 4.6.3) shows that salicylic has one ionizable proton (carboxylic proton) in the pH range of this study while the second proton from the OH group remain bound to the ligand. The proton from the carboxylic group, LH_2, gets fully deprotonated at pH 6 leaving the LH species to be the only existing species at the physiological pH (i.e. pH 7.4), with 100 % mole fraction.

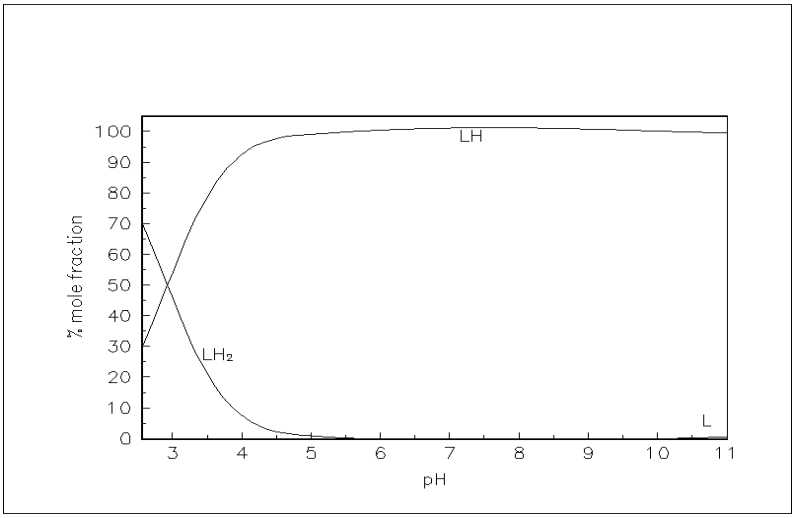

***Figure 4.6.3**: Speciation distribution curve for the protonation of salicylic acid plotted as a function of pH at 25 °C and 0.15 M NaCl. Concentrations used were 0.003324 M salicylic acid and 0.008391 M HCl.*

4.6.4 Complexation of Zr(IV) with salicylic acid

In the complexiometric titrations of Zr(IV)-salicylic acid, better models were obtained from using 1:1 and 2:1 ligand to metal concentration ratios. Only two sets of points from the titration data were used because of the precipitation which formed when the metal/ligand concentration was increased. The $\overline{Z}$ curves (Figure 4.6.4) also showed some evidence of hydrolysis indicated by the back fanning.

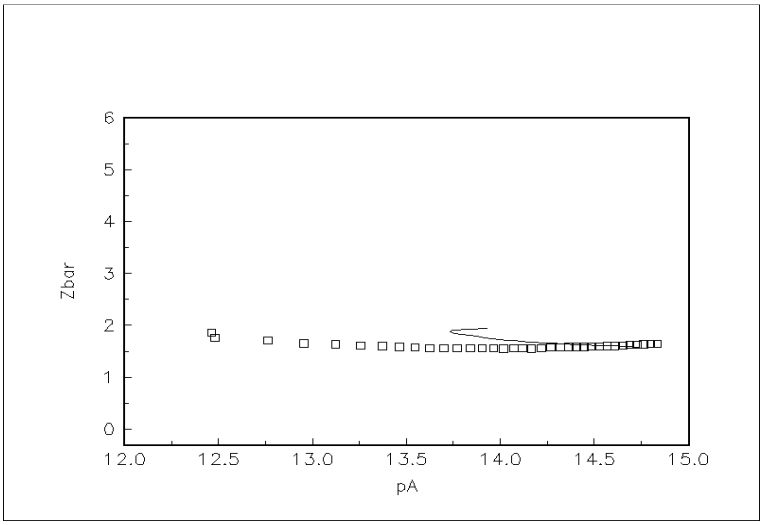

***Figure 4.6.4**: $\overline{Z}$ curve for the complexation of salicylic acid with Zr(IV). Experimental (2:1 (□)) and theoretical (line) formation for Zr(IV) complexation by salicylic acid. The titration represented by (□) 0.001969 M salicylic acid, 0.0010021M Zr(IV) 0.0125023 M HCl.*

From deprotonation curves, $\overline{Q}$ for Zr(IV)-salicylate (Figure 4.6.5), the occurrence of hydroxo and mixed hydroxo complexes can also be deduced. For this system, the $\overline{n}$ is also below the $\overline{Q}$ throughout the titrations.

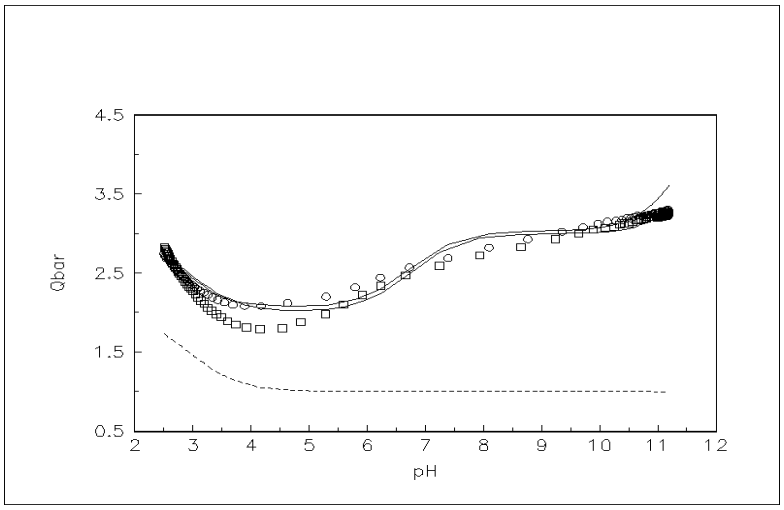

***Figure 4.6.5**: $\overline{Q}$ curves for the complexation of salicylic acid with Zr(IV). Experimental (1:1 (O) and 2:1 (□)) and theoretical (lines) deprotonation formation curves for Zr(IV) complexation by salicylate. The two separate titrations are represented by (O) 0.0009837 M salicylic acid, 0.0010011 M Zr(IV), 0.0124966 M HCl and (□) 0.0019693 M salicylic acid, 0.0010021 M Zr(IV), 0.0125023 M HCl.*

The speciation curves of Zr(IV)-salicylate is shown in Figure 4.6.6. These curves represent various species present from low to high pH throughout the titrations, which are only mixed hydroxo complexes, MLH_{-1}, $MLH_{-2,}$ and MLH_{-3}. The MLH_{-1} species appears to be predominant in the acidic pH region, pH < 6.5. The MLH_{-2} species are also the predominate species at the physiological condition with 60 % mole fraction and the remaining 40 % belonging to MLH_{-1}. The MLH_{-3} species only starts forming at pH 9.5.

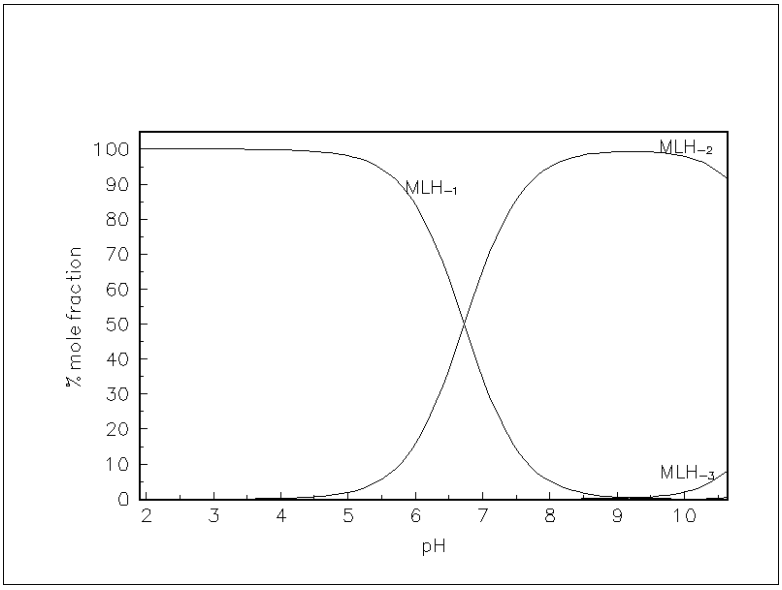

Figure 4.6.6*: Speciation distribution curve of Zr(IV) complexation by salicylate plotted as a function of pH at 25 °C and 0.15 M ionic strength. Concentrations used were 0.0019693 M salicylic acid, 0.0010021 M Zr(IV), 0.0125023 M HCl.*

The MLH_{-2} species starts to form at pH 3.5 (Figure 4.6.6), which is the region that deviation between the two data curves becomes visible in the $\overline{Q}$ curves (Figure 4.6.5). These deviations in the curves come as a result of the formation of a precipitate which was observed during the experiment. The precipitate was only observed in the 2:1 ligand to metal ratio titration, which explains why it is in this curve that the deviation from the theoretical curve is observed. Although the 1:1 ligand to metal ratio curve appears to follow the theoretical curve closely, it also has its maximum deviation in a similar manner as the amino acids, glutaminate, aspartate and asparaginate, as discussed. It shows maximum deviation at pH 8 where the MLH_{-2} species has its maximum percent mole fraction.

4.7 CITRATE

4.7.1 Introduction

Citrate, the conjugate base of citric acid (Figure 4.6.1) plays an important role in the synthesis of fatty acids. Citric acid functions as an anticoagulant and alkalinising agent in blood; it prevents the blood from clotting and balances blood pH by reducing it [20].

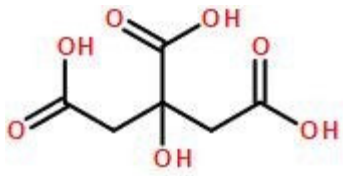

***Figure 4.7.1**: Structure of citric acid*

The structure (Figure 4.7.1) shows that citric acid has three ionizable (three carboxylic groups or $R–COO^-$ functional groups) protons therefore it is a polyprotic acid. Polyprotic acids are able to donate more than one proton. The pK_a values of these acids always increase successively because it becomes more difficult to stabilize the additional electron density that results after each proton donated [21]. The structure of citric acid also allows one to predict that the acid group in the middle will have the lowest pK_a because the hydroxyl group also bonded to the middle carbon is electron-withdrawing *by induction*.

4.7.2 Results and discussions

The results of modelling using the computer program ESTA are given in Table 4.6. The low Hamilton R factors indicate that the models generated were good fits. The constants obtained closely resemble the values reported in the literature [13].

Table 4.6: Protonation constants of citric acid and equilibrium constants of Zr(IV) complexation with citric acid as determined by glass electrode potentiometry and ESTA modelling at 25 °C and ionic strength of 0.15 mol.dm^{-3} NaCl.

***Equilibrium Species*[#]**	**Log β (*25 ºC*)**		**Hamilton R-factor**	**Number of points**
	This work	Literature[13]		
	0.15 M NaCl	*0.1 M NaCl*		
Citric acid				
$H + L \rightleftharpoons HL$	5.71 ± 0.01	5.67 ± 0.03	0.02407	243
$2H + L \rightleftharpoons H_2L$	4.33 ± 0.01	4.35 ± 0.05		
$3H + L \rightleftharpoons H_3L$	2.91 ± 0.02	2.90 ± 0.06		
$Zr(IV) - H \rightleftharpoons Zr(IV)H_{-1}$	0.51			
$Zr(IV) - 5H \rightleftharpoons Zr(IV)H_{-5}$	-14.95			
$3Zr(IV) - 4H \rightleftharpoons Zr(IV)H_{-4}$	0.24			
$4Zr(IV) - 8H \rightleftharpoons Zr(IV)H_{-8}$	-4.32			
$M + L - H \rightleftharpoons MLH_{-1}$	26.06 ± 0.07		0.04472	260
$M + L - 2H \rightleftharpoons MLH_{-2}$	18.07 ± 0.05			

[#] *The charges on Zr(IV) ions, citrate, protons and complexes are omitted for simplicity.*

** Hydrolysis constants for Zr(IV) are obtained from literature [14] and included in the model. They are expressed as ZrH_{-x} instead of the normal $Zr(OH)_x$ because the ESTA program uses this format as input.*

4.7.3 Citric acid protonation (ionization)

The protonation curve for citric acid is shown in Figure 4.7.2. The calculated data, $\overline{Z}_H$ (represented by the solid line) follows the experimental data (points) very closely.

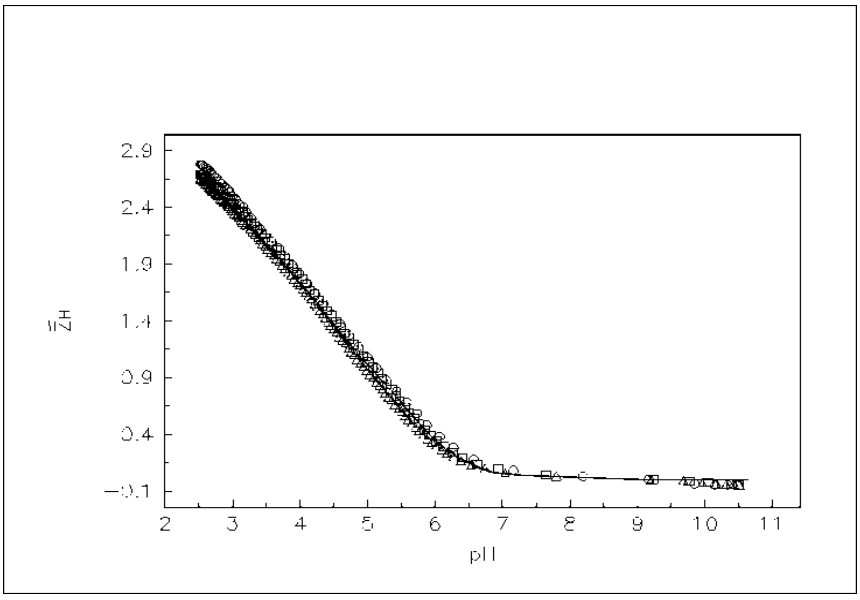

***Figure 4.7.2**: $\overline{Z}_H$ curves for the protonation of citric acid. Experimental (symbols) and theoretical (lines) protonation formation curves for citric acid. The titrations are represented by (O) 0.00166023 M citric acid, 0.00833667 M HCl, (□) 0.00332367 M citric acid, 0.00838278 M HCl and (Δ) 0.00499033 M citric acid, 0.00842460 M HCl.*

The citric acid in this study also proved to have three ionisable protons. This is also illustrated in the species distribution in Figure 4.7.3. In a highly acidic solution, the ligand exists in the fully protonated form as LH_3. On increasing the pH, the ligand loses its protons, LH_3, LH_2 and LH successively, more or less in the acidic region. This is expected because all the ionizable protons belong to acidic carboxyl groups. At the physiological pH (pH 7.4), there is only 3 % mole fraction of LH with the remaining 97 % belonging to the free ligand L.

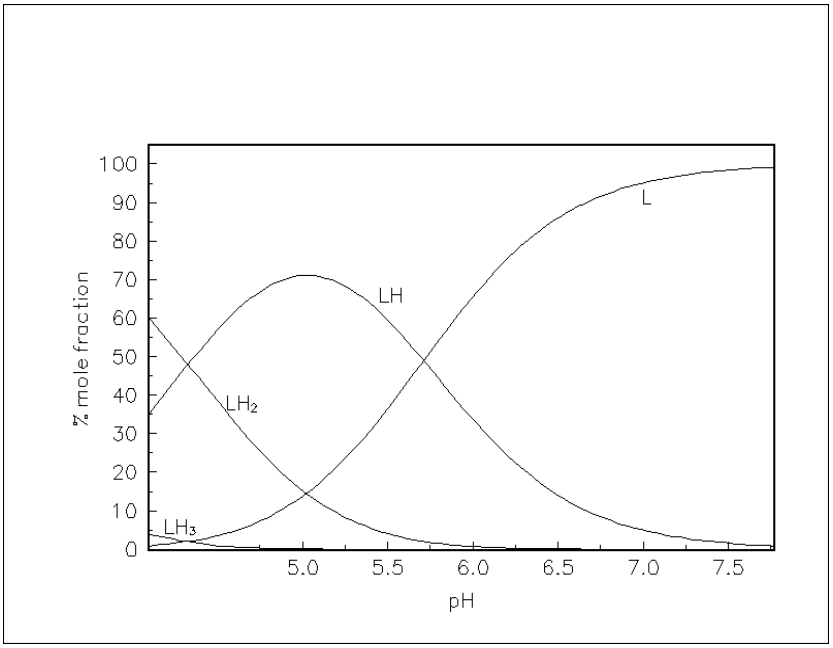

***Figure 4.7.3**: Speciation distribution curve for the protonation of citric acid plotted as a function of pH at 25 °C and 0.15 M NaCl. Concentrations used were 0.00499033 M citric acid and 0.00842460 HCl.*

4.7.4 Complexation of Zr(IV) with citric acid

In the complexiometric titrations of Zr(IV)-citrate good models were also obtained from using higher ligand to metal concentration ratios (2:1, 3:1, and 4:1). The modelled curves of the $\overline{Z}$ curves (Figure 4.7.4) also showed some evidence of hydrolysis by back fanning at low pA (negative logarithm of the free ligand concentration), indicating the presence of hydroxo and mixed hydroxo complexes.

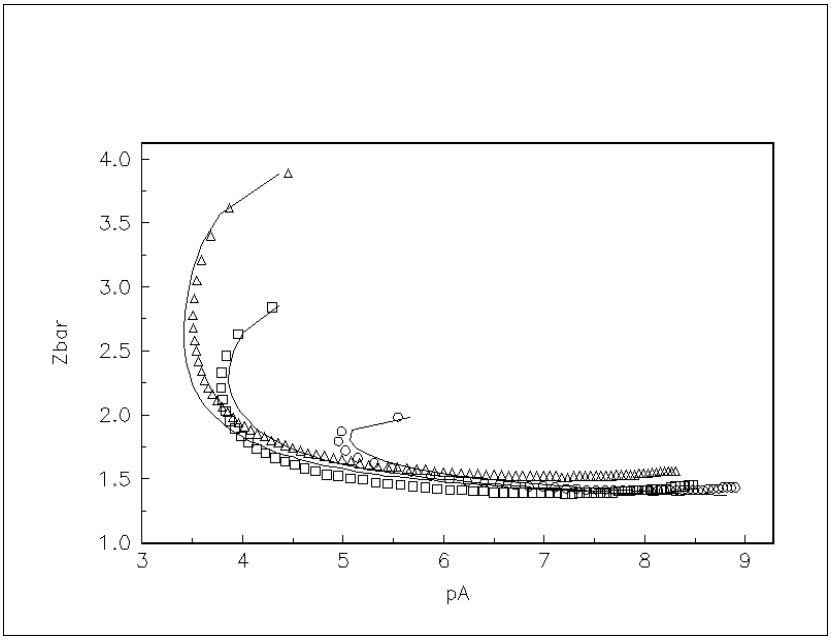

***Figure 4.7.4**: $\overline{Z}$ curves for the complexation of citrate with Zr(IV). Experimental (2:1 (O), 3:1 (□) and 4:1 (Δ)) and theoretical (lines) formation for Zr(IV) complexation by citric acid. The three separate titrations are represented by (O) 0.0019892 M citric acid, 0.0009913 M Zr(IV), 0.0126450 M HCl, (□) 0.0029568 M citric acid, 0.0009923 M Zr(IV), 0.0124373 M HCl and (Δ) 0.0039962 M citric acid, 0.0010041 M Zr(IV), 0.0126964 M HCl.*

The $\overline{Q}$ curves (Figure 4.7.5) for this model are also above the $\overline{n}$ which also indicates that more free protons from the system are being detected at the glass electrode. This comes from either deprotonation of coordinated water (formation of hydroxy species) or the ligand loses more protons. It can also be observed that even though there is evidence of Zr(IV)-citrate complexes forming, the protonation curve of the free ligand and the metal-ion complexation are not that well distinguished. The inflection point that is seen at pH 6.8 can be attributed to the start of complexation because in the region pH < 6.8, the $\overline{Q}$ curves run parallel to the $\overline{n}$ indicating no detectable complexation taking place .

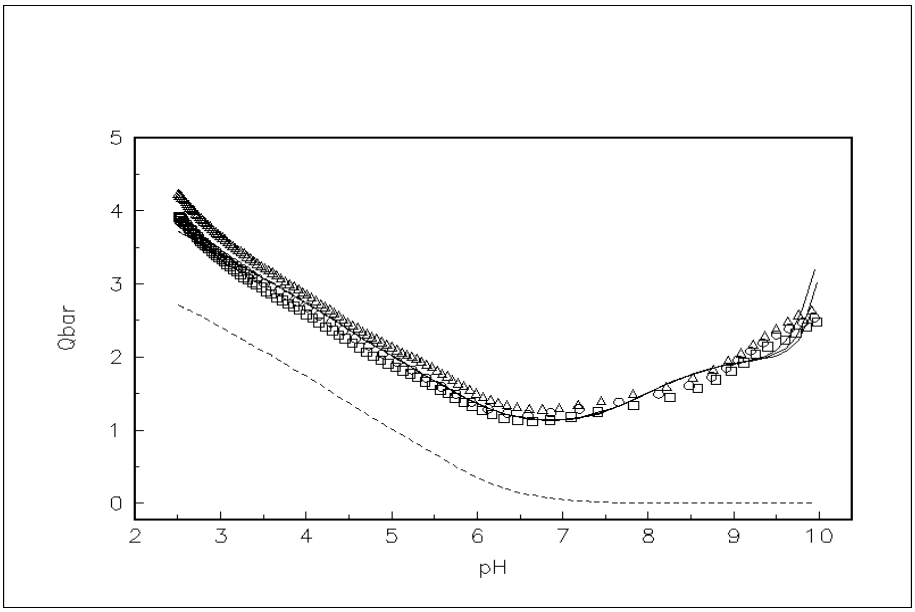

Figure 4.7.5: *$\overline{Q}$ curves for the complexation of citrate with Zr(IV). Experimental (2:1 (O), 3:1 (□) and 4:1 (Δ)) and theoretical (lines) deprotonation formation curves for Zr(IV) complexation by citric acid. The three separate titrations are represented by (O) 0.0019892 M citric acid, 0.0009913 M Zr(IV), 0.0126450 M HCl, (□) 0.0029568 M citric acid, 0.0009923 M Zr(IV), 0.0124373 M HCl and (Δ) 0.0039962 M citric acid, 0.0010041 M Zr(IV), 0.0126964 M HCl. All solutions were at 25 °C and 0.15 M ionic strength.*

The speciation curves of Zr(IV)-citrate (Figure 4.7.5) represent various species present from low to high pH throughout the titrations, namely MLH_{-1}, MLH_{-2} and MH_{-5}. The MLH_{-1} species appears to be predominant across most of the region in the pH of the study, (i.e. 2 < pH > 8). It is then followed by the notorious MLH_{-2} which is predominant in the region 8 < pH > 10. Similarly to the amino acids and salicylic acid discussed, MLH_{-2} forms after the dissociation of the carboxylic protons which provide a possible site for complexation.

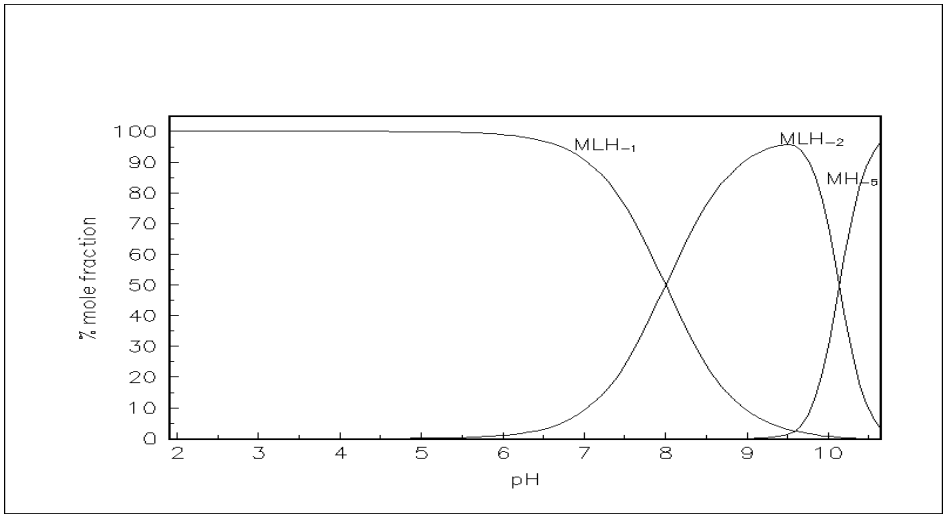

***Figure 4.7.6**: Speciation distribution curve of Zr(IV) complexation by citrate plotted as a function of pH at 25°C and 0.15 M ionic strength. Concentrations used were 0.0029568 M citric acid, 0.0009923 M Zr(IV) and 0.0124373 M HCl.*

The formation of this species, MLH_{-2}, contributes to the data deviation from the theoretical curve at pH 9 in the $\overline{Q}$ curves (Figure 4.7.5). There is also another deviation at the end, due to the precipitation of the Zr(IV) ion in the formation of the hydroxo complex, MH_{-5}.

4.8 DEFEROXAMINE

4.8.1 Introduction

The chelating agent chosen for this study, deferoxamine (Figure 4.8.1), known as DFO, DFOA, desferrioxamine-B, desferoxamine B, DFB-B or desferal: N'-{5-[acetyl(hydroxy)amino]-pentyl}-N-[5-({4-[(5-aminopentyl)(hydroxy)amino]-4-oxobutanoyl}amino)pentyl]-N-hydroxysuccin-amide, is a bacterial siderophore produced by the actinobacteria *Streptomyces pilosus* [22]. This siderophore is an iron chelator used for treating patients with iron overload diseases [22].

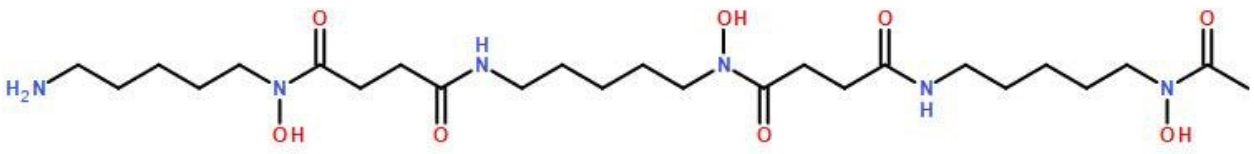

***Figure 4.8.1**: Structure of Deferoxamine*

The structure (Figure 4.8.1) shows the four dissociable protons of deferoxamine; three belonging to the hydroxamate binding groups and one from the primary amine group.

4.8.2 Results and discussions

The results of modelling using the computer program ESTA are given in Table 4.7. The low Hamilton R factors indicate that the models generated were good fits. The constants obtained also resemble the values reported in the literature [23].

Table 4.7: Protonation constants of Desferrioxamine B (DFO-B) and equilibrium constants of Zr(IV) complexation with DFO-B as determined by glass electrode potentiometry and ESTA modelling at 25 °C and ionic strength of 0.15 mol.dm^{-3} NaCl.

Equilibrium Species [#]	**Log β (*25 ºC*)**		**Hamilton R-factor**	**Number of points**
	This work	Literature[13]		
	0.15 M NaCl	*0.1 M $NaNO_3$*		
DFO-B				
H + L ⇌ HL	9.52 ± 0.05	9.70	0.07519	237
2H + L ⇌ H_2L	9.12 ± 0.04	9.03		
3H + L ⇌ H_3L	8.39 ± 0.04	8.39		
Zr(IV) - H ⇌ Zr(IV)H_{-1}	0.51			
Zr(IV) - 5H ⇌ Zr(IV)H_{-5}	-14.95			
3Zr(IV) - 4H ⇌ Zr(IV)H_{-4}	0.24			
4Zr(IV) - 8H ⇌ Zr(IV)H_{-8}	-4.32			
M + L+ H ⇌ MLH	50.36 ± 0.09		0.01915	224
M + L ⇌ ML	39.51			

[#] *The charges on Zr(IV) ions, DFO-B, protons and complexes are omitted for simplicity.*

** Hydrolysis constants for Zr(IV) are obtained from literature [14] and included in the model. They are expressed as ZrH_{-x} instead of the normal $Zr(OH)_x$ because the ESTA program uses this format as input.*

4.8.3 DFO-B protonation (ionization)

The protonation curve for DFO-B is shown in Figure 4.8.2. The calculated data (represented by the solid line) follows the experimental data (points) very closely.

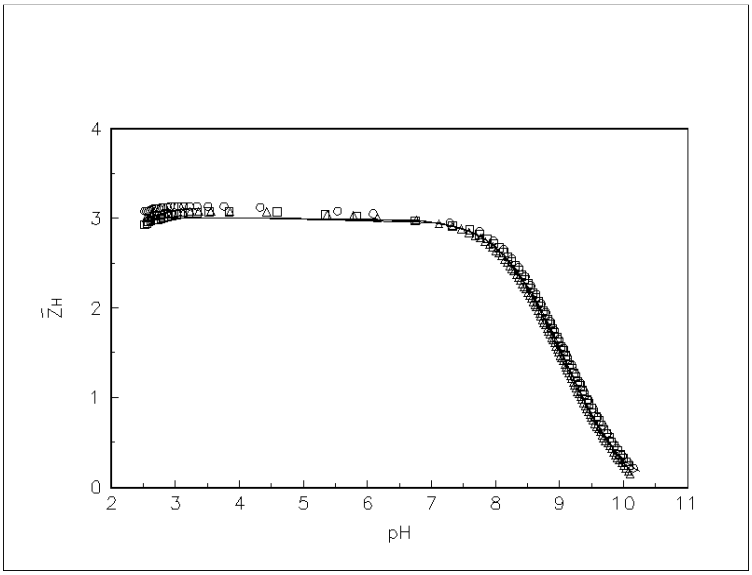

***Figure 4.8.2**: $\overline{Z}_H$ curves for the protonation of DFO-B. Experimental (symbols) and theoretical (lines) protonation formation curves for DFO-B. The titrations are represented by (O) 0.00166023 M DFO-B, 0.00842667 M HCl, (□) 0.00332367 M DFO-B, 0.00843481 M HCl and (Δ) 0.00499033 M DFO-B, 0.00841458 M HCl.*

Although the fully protonated desferoxamine B (H_4DFO-B) contains four dissociable protons, only three proton dissociation constants could be measured in the experimental pH range. This is because the deprotonation constant of the primary amine group occurs at the limit of the pH accessible to potentiometric measurements. Therefore, by taking into account the deprotonation sites of DFO-B accessible in the pH range of this study, the fully protonated ligand is denoted H_3DFO-B. This is why the $\overline{Z}_H$ curves (Figure 4.8.2) and the speciation distribution diagram (Figure 4.8.3) show that the ligand loses three protons.

The speciation distribution diagram (Figure 4.8.3) show that in acidic solution (pH < 6.8), the ligand exists in the fully protonated form as LH_3. On increasing pH, the species (LH_3) loses its

protons forming LH_2 which becomes the predominant species in the region 8.5 < pH > 9.1.The ligand therefore exists as LH_3 constituting more than 80 % concentration and LH_2 constituting about 10 % concentration at the physiological pH(i.e. pH 7.4). The third and last protonated form (LH) starts deprotonation at pH > 7.8 forming the fully deprotonated ligand (L) which is the predominant species at pH > 9.5.

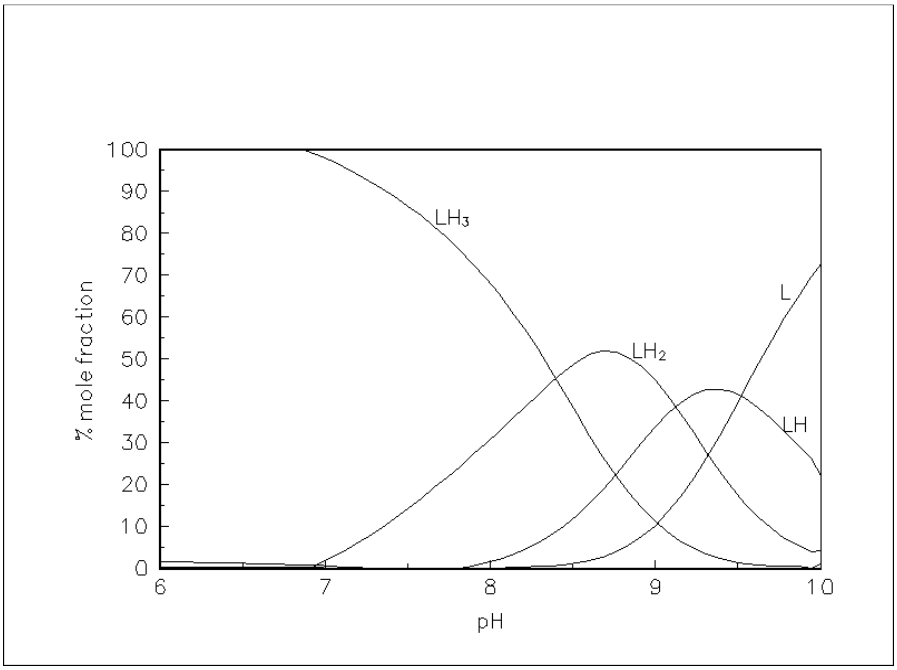

Figure 4.8.3*: Speciation distribution curve for the protonation of DFO-B plotted as a function of pH at 25 °C and 0.15 M NaCl. Concentrations used were 0.00166023 M DFO-B and 0.00842667 M HCl.*

4.8.4 Complexation of Zr(IV) with DFO-B

In the complexiometric titrations of Zr(IV)-DFO-B good models were also obtained from using higher ligand to metal concentration ratios (2:1, 3:1, and 4:1).The modelled curves of the $\overline{Z}$ curves (Figure 4.8.4) did not show evidence of hydrolysis, but instead they showed the presence of one major species which dominated over most of the pA range being studied.

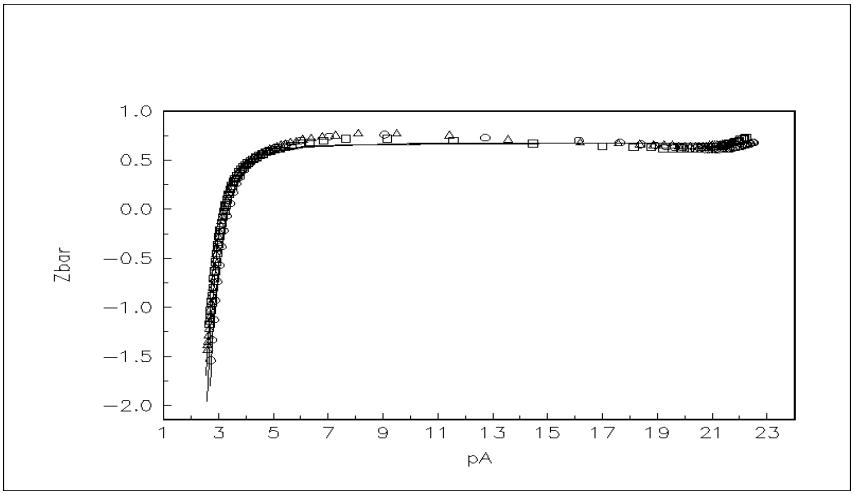

***Figure 4.8.4**: $\overline{Z}$ curves for the complexation of DFO-B with Zr(IV). Experimental (2:1 (O), 3:1 (□) and 4:1 (Δ)) and theoretical (lines) formation for Zr(IV) complexation by DFO-B. The three separate titrations are represented by (O) 0.0019892 M DFO-B, 0.0010129 M Zr(IV), 0.0125871 M HCl, (□)0.0029568 M DFO-B, 0.0009923 M Zr(IV), 0.0121003 M HCl and (Δ) 0.0039862 M DFO-B, 0.0010041 M Zr(IV) 0.0128011 M HCl.*

The deprotonation function $\overline{Q}$ curves (Figure 4.8.5) does not intersect with the n-bar, therefore there is no hydroxo or mixed hydroxo complexes present in the pH range 2.5-10. The function shows that at the start of the titration, at a pH 2.5, the $\overline{Q}$ is greater than zero, indicating that complexation has begun. The function remains constant in the pH range 2.5-10 thus indicating the presence of a single stable complex. This complex can be deduced; In the presence of the metal ion, two protons are lost by the ligand on complexation per metal ion therefore the complex that forms is

$$M + LH_3 - 2H \rightleftharpoons MLH \qquad (4.8)$$

Between pH 8-10 there is a reduction in $\overline{Q}$ indicting the formation of a new complex. This new complex can be deduced at pH 9 where $\overline{Q}$ is zero and the ligand has lost its third proton; In the presence of the metal ion, three protons are lost by the ligand on complexation per metal ion in the complex that forms is

$$M + LH_3 - 3H \rightleftharpoons ML \qquad (4.9)$$

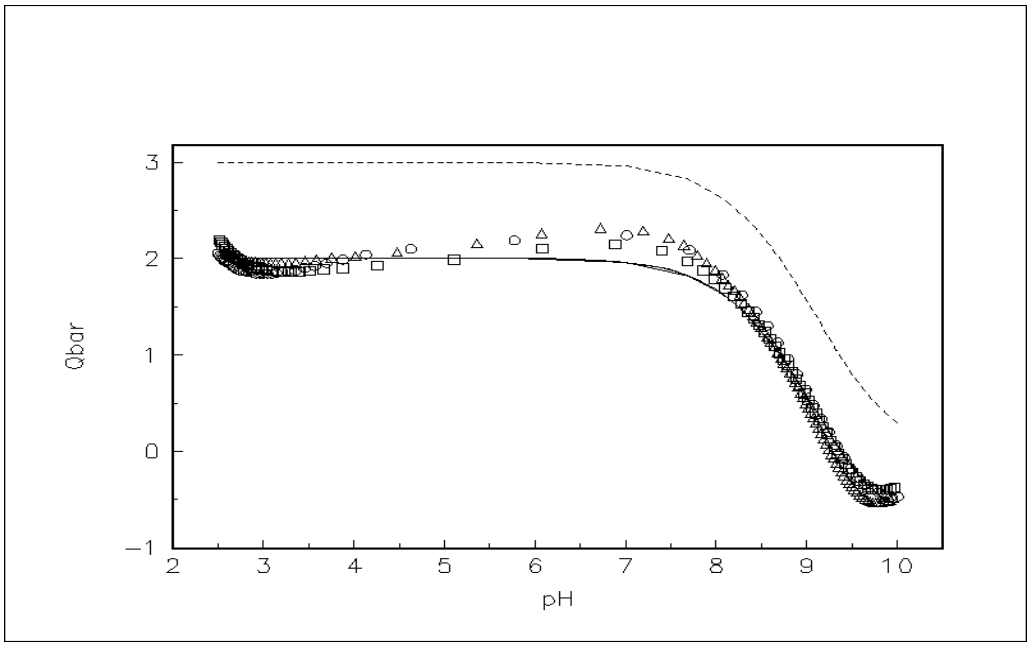

***Figure 4.8.5**: $\overline{Q}$ curves for the complexation of DFO-B with Zr(IV). Experimental (2:1 (O), 3:1 (□) and 4:1 (Δ)) and theoretical (lines) deprotonation formation curves for Zr(IV) complexation by DFO-B. The three separate titrations are represented by (O) 0.0019892 M DFO-B, 0.0010129 M Zr(IV) 0.0125871 M HCl, (□) 0.0029568 M DFO-B, 0.0009923 M Zr(IV) 0.0121003 M HCl and (Δ) 0.0039862 M DFO-B, 0.0010041 M Zr(IV) 0.0128011 M HCl.*

The species distribution curves (Figure 4.8.6) shows that the dominant species in this system is indeed the MLH species which has a 100 % mole fraction in the pH region extending from 2 to 8. Therefore it is the only species present at the physiological pH (i.e. 100 % mole fraction). The ML species on the other hand only starts to form at pH 8 reaching a maximum of 15 % mole fraction at pH 10.3, followed by the formation of MH_{-5} which suggests that the ligand is fully deprotonated and no longer has protons to donate for complexation.

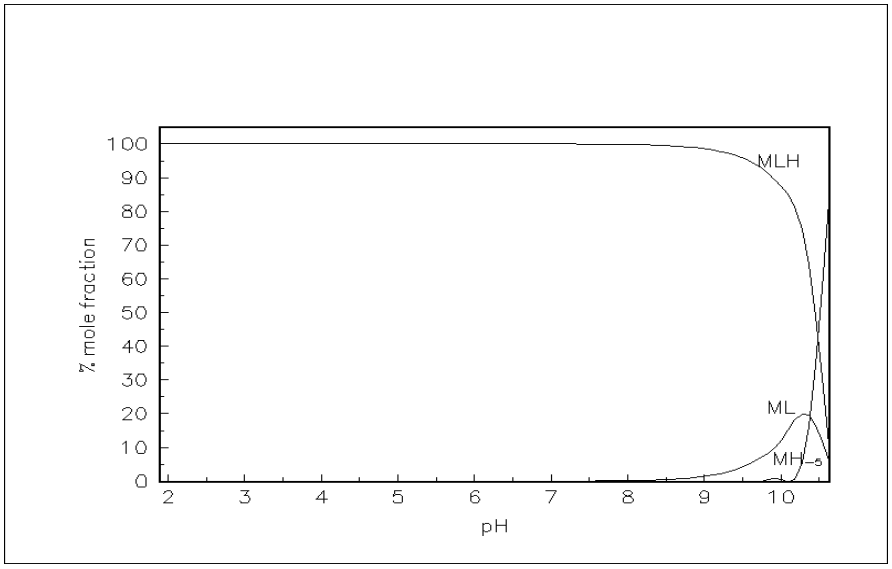

***Figure 4.8.6**: Speciation distribution curve of Zr(IV) complexation by DFO-B plotted as a function of pH at 25 °C and 0.15 M ionic strength. Concentrations used were 0.0039862 M DFO-B, 0.0010041 M Zr(IV) and 0.0128011 M HCl.*

The deviation of the theoretical curve and the experimental points in the pH region 4-8 of $\overline{Q}$ curves (Figure 4.8.5) can therefore be attributed to the hydrolysis of the metal ion in the formation of the MLH species in a similar behaviour seen in the other ligands discussed in this investigation.

4.9 BLOOD PLASMA SIMULATIONS

4.9.1 Introduction

DFO-B will form more stable complexes in the blood with Zr(IV) than all the other ligands discussed in this investigation because its predominant species (MLH) has a higher formation constant at the physiological pH. The notable distinction between ZrHDFO-B and the plasma ligand complexes (Figure 4.9.1) was therefore theoretically expected.

4.9.2 Speciation in blood plasma

The speciation of Zr^{4+} in normal blood plasma, in the presence of DFO-B (Figure 4.9.1) shows that 99.7 % mole fraction of the metal ion will not dissociate from the Zr^{4+}-DFO-B complex. Of the 0.3 % dissociated mole fraction of the metal ion, $Zr(OH^-)_2$ GLN and $Zr(OH^-)$CTA species constitutes a 0.1 % mole fraction each.

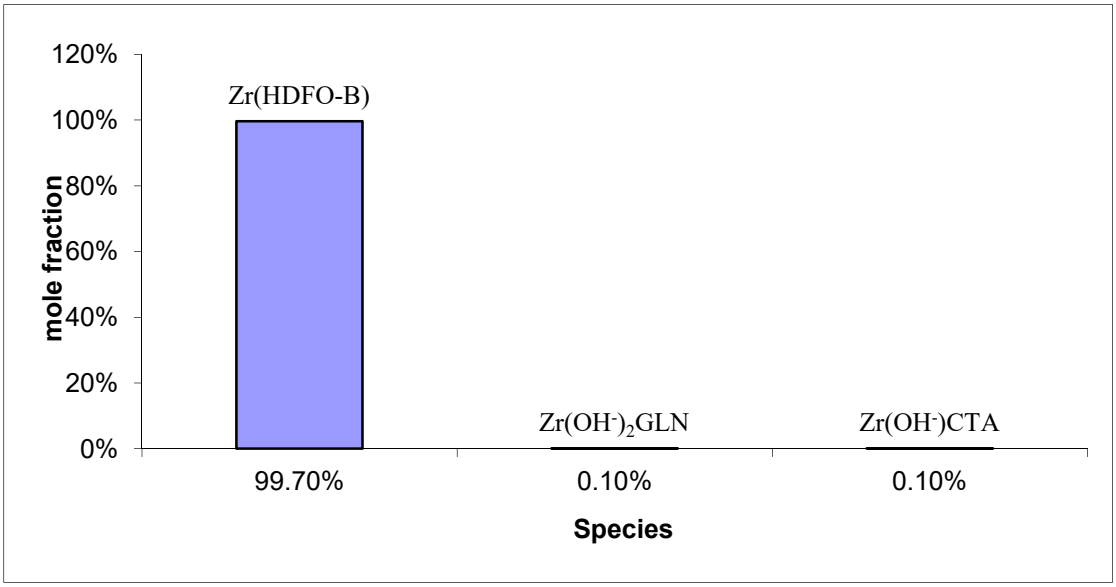

***Figure 4.9.1**: Speciation of Zr^{4+} in normal blood plasma, in the presence of DFO-B. Concentrations used were M:L of 1:10 (i.e. $[Zr^{4+}] = 8.5 \times 10^{-6}$ mol.dm^{-3} and [DFO-B] = 8.5×10^{-5} mol.dm^{-3}).*

Although most of the Zr^{4+} does not dissociate from the Zr^{4+}-DFO-B complex, only 10 % mole fraction of the complex remains intact due to the dissociation of the ligand (Figure 4.9.2). As much as 88.6 % mole fraction of DFO-B dissociates to form a Fe^{3+}-DFO-B complex. This is not surprising because DFO has functional groups which have strong binding affinity for Fe^{3+} [23]. The other complexes that results from the dissociation of DFO-B are H_3DFO-B, $Fe(OH^-)$DFO-B and H_2DFO-B. They only occupy 1.5 % mole fraction of the total mole ratio.

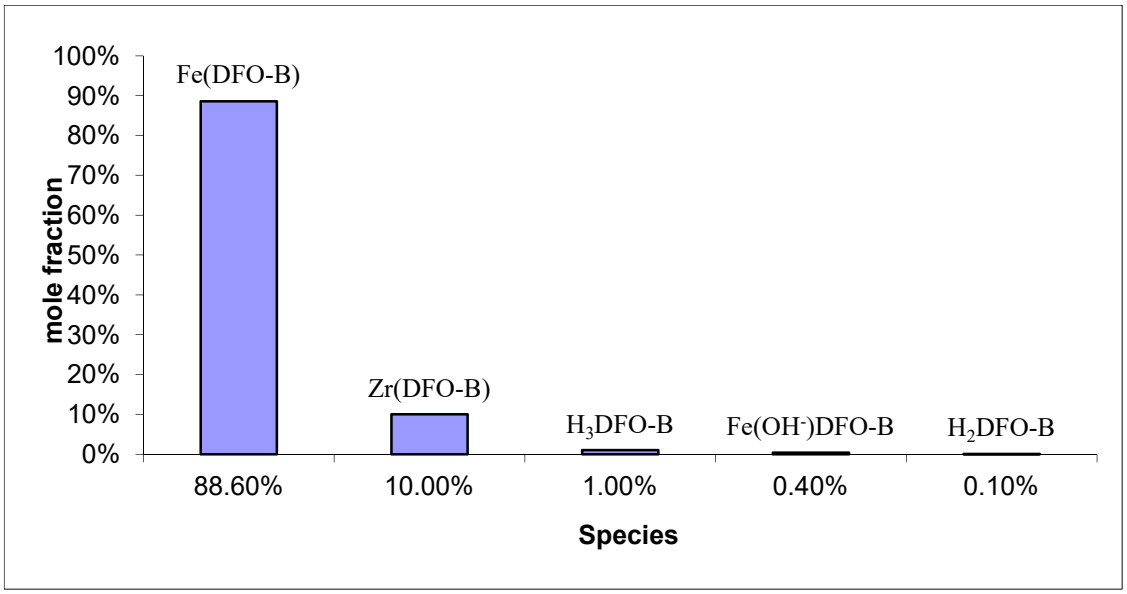

***Figure 4.9.2**: Speciation of DFO-B in normal blood plasma, in the presence of Zr^{+} . Concentrations used were M:L of 1:10 (i.e. $[Zr^{4+}] = 8.5 \times 10^{-6}$ mol.dm^{-3} and [DFO-B] = 8.5×10^{-5} mol.dm^{-3}).*

4.9.3 Blood plasma mobilization indexes

The simulated PMI curves (Figure 4.9.3) shows that when DFO is administered at a concentration of 8.5×10^{-5} mol.dm^{-3} (a 1:10 metal ion to ligand ratio), the ligand will present a substantial influence on the metal ion balance present in blood plasma. The ligand concentration of 8.5×10^{-5} mol.dm^{-3} and 1:10 metal ion to ligand ratio were chosen because they are typical biological concentrations of metal ions and ligands [24]. A significant mobilization can be observed on Fe^{3+}. This is expected because DFO-B has been used to treat patients from the effects of iron overload [23]. Ca^{2+} and Mg^{2+} are not mobilised at all within blood plasma, whereas Cu^{2+} and Zn^{2+} are mobilized by less than significant amounts. This result suggests that patients may develop iron deficiency anaemia during a treatment regime. Also because the treatment regime would have to be prolonged to account for the rapid elimination of DFO from the bloodstream, that is, it has a 5-10 minutes elimination half life, the iron deficiency will be severe on patients [25]. The use of ^{89}Zr-DFO-B would therefore require the co-administration of sufficient Fe^{3+} supplements to counter the effect of iron mobilization induced by the presence of the ligand in the body.

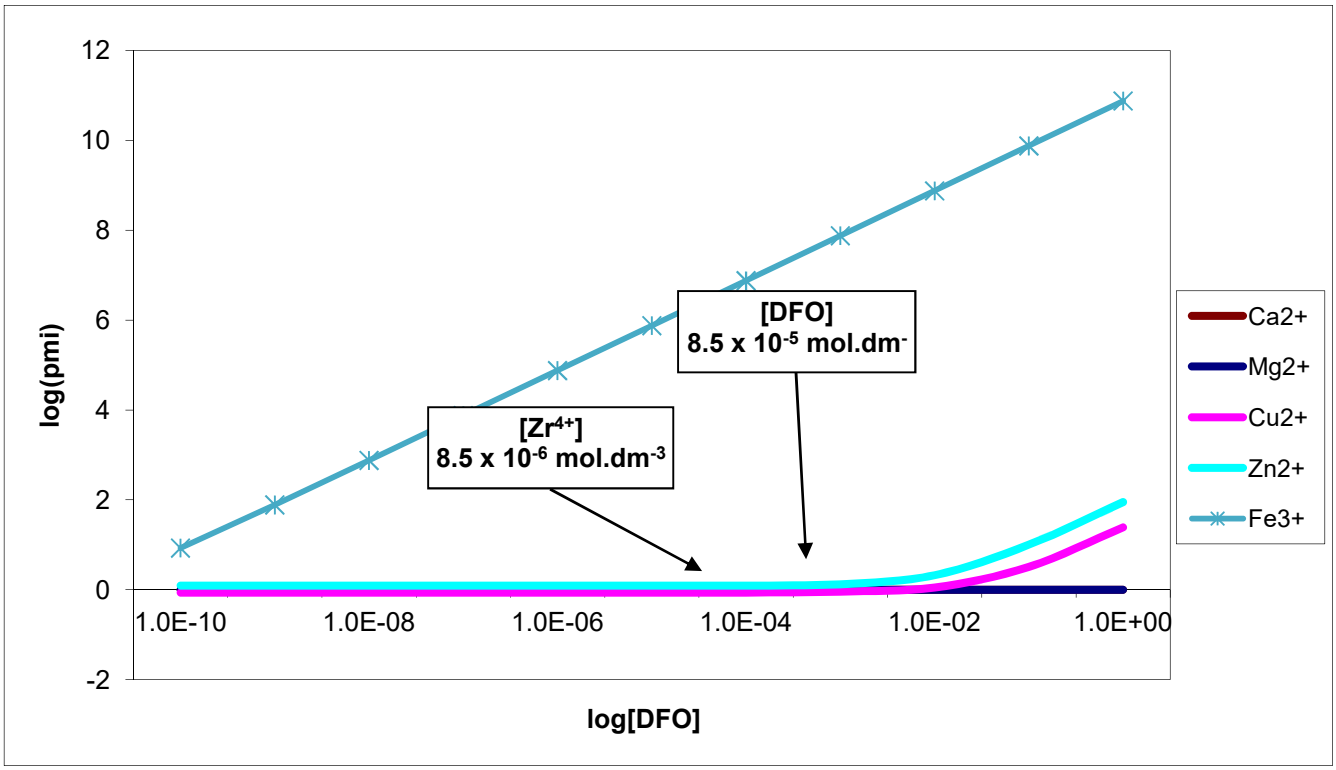

***Figure 4.9.3**: Blood plasma mobilization index (PMI) curves of Zr-DFO-B complex for Fe^{3+}, Cu^{2+}, Ca^{2+}, $Mg^{2+}$and Zn^{2+}*

REFERENCES

[1] Deri MA, Zeglis BM, Francesconi LC, Lewis JS. PET imaging with ^{89}Zr: From radiochemistry to the clinic. Nucl Med Bio 2013;40:3-14.

[2] Adair JH, Krarup H, Venigalla S, Tsukada T. A review of the aqueous chemistry of the zirconium-water system to 200 °C. Invited paper in Aqueous Chemistry and Geochemistry of Oxides, Oxyhydroxides, and Related Materials, 1996, p, 1-12.

[3] Clark J. Complex metal ions- The acidity of the hexaaqua ions. Chemguide.co.uk 2003.

[4] Landen K. Antiperspirants and deodorants, 2nd Edition. Cosmetic Science and Technology 1999;20:139.

[5] Suwardi, Pranowo HD, Armunanto R. Structure and dynamics of Zr^{4+} in aqueous solution: An AB initio QM/MM molecular dynamics study. Indones J Chem 2015;15:155-162.

[6] Gabanamotse K. The complexation of selected blood plasma ligands with Sn(IV) used to predict the in vivo behaviour of Sn(IV)-PEI-MP. NWU, MSc Thesis, 2007, p, 49.

[7] Sharma RK. A Textbook of Coordination Chemistry. Discovery Publishing Company, New Delhi, 2007, p, 9.

[8] Morel FMM, Hering JG. Principles and Applications of Aquatic Chemistry. John Wiley & Sons, Canada, 1993, p, 322.

[9] Alberts B, Johnson A, Lewis J, Raff M, Roberts K, Walters P. Molecular Biology of the Cell, 4th Edition. Garland Science, New York 2002.

[10] Tropp BE. Molecular Biology: Genes to Proteins, 4th Edition. Jones & Bartlett Learning, LLC 2012.

[11] Bindu GH, Rao GN. Effect of anionic micelles on speciation of L-glutamine in presence/absence of metals. Chemical Speciation and Bioavailability 2011;23:88-95.

[12] Wade LG. Organic Chemistry, 7th Edition. Pearson Education, Inc 2010.

[13] Martell AE, Smith RM. Critical Stability Constants, Other Organic Ligands. Plenum press, New York, Vol. 3, 1977.

[14] Martell AE, Smith RM. Critical Stability Constants, Inorganic complexes. Plenum press, New York, Vol. 4, 1989.

[15] Betts MJ, Russell RB. Amino acid properties and consequences of substitutions. In Bioinformatics for Geneticists, M.R. Barnes, I.C. Gray eds, Wiley 2003.

[16] Athota CL, Valluri RK, Gollapalli NR. Chemical speciation of divalent metal complexes of L-aspartic acid propylene glycol-water mixture. J of Advanced Electrochem 2015:1;5–8.

[17] Wetzler M, Sanford BL, Kurtzberg J, DeOliveira D,Franke SR, et al. Effective asparagine depletion with pegylated asparaginase results in improved outcomes in adult acute lymphoblastic leukemia: cancer and leukemia group b study 9511. Blood 2007:109;4164.

[18] Toiu A, Vlase L, Ilioara O, Benedec D, Tamas M. HPLC analysis of salicylic derivatives from natural products. FARMACIA 2011;59:106.

[19] Young P. Salicylate. National Poisons Information Services, United Kingdom 2015. http://www.inchem.org/documents/ukpids/ukpids/ukpid14.htm[Accessed on 29 Dec 2015].

[20] Ranby M, Sundell IB, Nilsson TK. Blood collection in strong acidic citrate anticoagulant used in a study of dietary influence on basal tPA activity. Thromb Haemost 1989:62;917-22.

[21] Soderberg T. Organic Chemistry with a Biological Emphasis Volume I. University of Minnesota, Morris Digital Well, Paper 1, 2010, p, 306.

[22] Chiani M, Akbarzadeh A, Farhangi A, Manzinani M,Saffari Z, et al. Optimization of culture medium to increase the production of desferrioxamine B (Desferal) in Streptomyces pilosus. Pak J Biol Sci 2010:13;546-50.

[23] Boukhalfa H, Reill SD, Neu MP. Complexation of Pu(IV) with natural Siderophore Desferrioxamine B and the redox properties of Pu(IV)(siderophore) complexes. Inorg Chem 2007;46:1018-1026.

[24] Gałęzowska J, Kafarski P, Kozłowski H, Młynarz P, Nurchi V, et al. N,N'-Ethylenediaminobis(benzylphosphonic acids) as a potent of metal ions. Inorganica Chimica: 2009:362;707-713.

[25] Crisponi G, Nurchi VM, Crespo-Alonso M, Sanna G, Zoroddu MA, Alberti G, et al. A speciation study on the perturbing effects of iron chelators on the homeostasis of essential metal ions. PLoS ONE 2015;10:7:e0133050.

CHAPTER 5: CONCLUSSION

The modelling of titration data by ESTA produced some reasonably satisfactory results with low Hamilton R-factors. The calculated functions ($\overline{Q}$, $\overline{Z}_H$ and $\overline{Z}_H$) were close to the experimental data, and the speciation distribution curves were obtained even though there was evidence of some poor complexing ability of the metal ion in the $\overline{Q}$ curves. There were some deviations in the theoretical and experimental $\overline{Q}$ curves with all the investigated ligands which proved that the metal hydrolysed before complexing. The formation constants of the species present were tabulated for all the systems. From these tables it can clearly be seen that that the stability constant for Zr(IV)-DFO-B is the highest at the physiological pH and this is a sign of sufficiently strong complexation in comparison to complexes formed between Zr(IV) and the blood plasma ligands studied. The higher formation constant proved that the Zr(IV)-DFO-B complex is able to withstand the competition from the studied blood plasma ligands and will not dissociate before it reaches the target. However, the ECCLES models on the other hand showed that even though the metal effectively binds to DFO-B, DFO-B has a stronger affinity for Fe(III) and this will result in the mobilization of the metal ion.

In conclusion, the Zr(IV)-DFO-B complex is a stable complex that can ensure that almost all of the ^{89}Zr ions reaches the targeted part of the body. This complex can therefore be the anticipated immuno-PET agent that can help in the fight against epithelial ovarian cancer. However, measures have to be taken to ensure that patients do not develop chronic Fe(III) deficiencies due to the mobilization of the metal ion facilitated by DFO. Another important conclusion that can also be drawn from this investigation is that the use of speciation studies is effective and this approach can reduce the number of clinical tests necessary to evaluate a proposed radiopharmaceutical.